ACS NANO

www.acsnano.org

ARTICLE

Schottky Junction Nanozyme Based on Mn-Bridged Co-Phthalocyanines and $Ti_3C_2T_x$ Nanosheets Boosts Integrative Type I and II Photosensitization for Multimodal Cancer Therapy

Fenghe Duan, Qiaojuan Jia, Gaolei Liang, Mengfei Wang, Lei Zhu, Kevin J. McHugh, Lihong Jing,* Miao Du,* and Zhihong Zhang*

Cite This: *ACS Nano* 2023, 17, 11290−11308

Read Online

ACCESS | Metrics & More | Article Recommendations | Supporting Information

ABSTRACT: **Cancer phototheranostics have the potential for significantly improving the therapeutic effectiveness, as it can accurately diagnose and treat cancer. However, the current phototheranostic platforms leave much to be desired and are often limited by tumor hypoxia. Herein, a Schottky junction nanozyme has been established between a manganese-bridged cobalt−phthalocyanines complex and $Ti_3C_2T_x$ MXene nanosheets (CoPc-Mn/$Ti_3C_2T_x$), which can serve as an integrative type I and II photosensitizer for enhancing cancer therapeutic efficacy *via* a photoacoustic imaging-guided multimodal chemodynamic/photothermal/photodynamic therapy strategy under near-infrared (808 nm) light irradiation. The Schottky junction not only possessed a narrow-bandgap, enhanced electron−hole separation ability and exhibited a potent redox potential but also enabled improved H_2O_2 and O_2 supplying performances *in vitro*. Accordingly, the AS1411 aptamer-immobilized CoPc-Mn/$Ti_3C_2T_x$ nanozyme illustrated high accuracy and excellent anticancer efficiency through a multimodal therapy strategy in *in vitro* and *in vivo* experiments. This work presents a valuable method for designing and constructing a multifunctional nanocatalytic medicine platform for synergistic cancer therapy of solid tumors.**

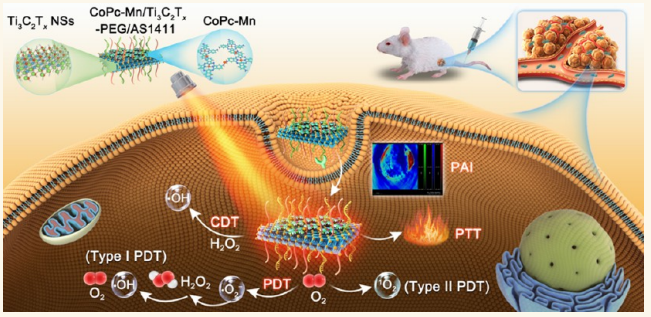

KEYWORDS: *multimodal cancer therapy, Schottky junction nanozyme, $Ti_3C_2T_x$ nanosheets, cobalt phthalocyanine, supply of O_2 and H_2O_2*

Cancer remains one of the most serious diseases that causes death in the world. Unfortunately, the current methods used to detect and treat cancer leave much to be desired. Theranostic platforms, which can be used to both accurately diagnose and treat cancer, have the potential to significantly prolong the survival of patients with cancer.[1−3] Phototherapies, such as photodynamic therapy (PDT) and photothermal therapy (PTT), are attractive on account of their noninvasiveness and ability to act locally and thereby avoid systemic toxicity.[4−6] PDT selectively produces reactive oxygen species (ROSs) from oxygen (O_2) utilizing photosensitizers (PSs) under light irradiation. These ROSs can become cytotoxic after reacting with proteins, DNAs, lipids, and other biological molecules, causing cancer cell death *via* distinct pathways.[7,8] There are two mechanisms for PDT: the type II PDT pathway of singlet oxygen ($^1O_2$) production by energy transfer[9] and the type I PDT pathway *via* the electron transfer or hydrogen abstraction to generate superoxide radical ($\cdot O_2^-$) and hydroxyl radical ($\cdot$OH). Also, the generated $\cdot O_2^-$ and $\cdot$OH species *via* the type I PDT mechanism not only can serve as oxidants for killing tumor cells but also can yield O_2 for recycling.[10] The type II PDT mechanism, which is feasibly performed in most current PDT

Received: December 9, 2022
Accepted: May 16, 2023
Published: June 5, 2023

https://doi.org/10.1021/acsnano.2c12270
ACS Nano 2023, 17, 11290−11308

PSs, is highly dependent on the O_2 level in the tissue environment,[11,12] whereas the type I pathway is less dependent on O_2,[13] rendering it largely unaffected by hypoxia within the tumor microenvironment (TME). To date, only a few photocatalysts, such as C_3N_4/MnO_2,[14] UMOF-TiO_2,[15] W_2C nanoparticles (NPs),[16] and TiO_2-N_3,[7] have demonstrated outstanding PDT performance *via* type I and II mechanisms. Thus, there is a need to identify multifunctional nanocatalysts that can overcome the PDT limitations to enhance PDT efficacy for tumors.[17] However, tumors are difficult to completely treat using a monotherapy due to low PDT efficiency in the hypoxic TME and the decreased immune response caused by the heat shock response of a mono-PTT method. In addition, cancer cells can also be killed *via* the chemodynamic therapy (CDT) mechanism *via* the generation of ·OH through the decomposition of hydrogen peroxide (H_2O_2) during *in situ* Fenton/Fenton-like reaction in the TME in the presence of metal ions,[18] while this strategy often suffers from a low H_2O_2 concentration in the TME, resulting in limited ·OH production.[19,20] To address this point and increase the efficiency of treatment,[21] different methods have been employed, such as catalyzing glucose to produce H_2O_2 by loading glucose oxidase (GO_x) to boost the H_2O_2 content in TME[22−24] or by loading antibody of vascular endothelial growth factor to restrain tumor angiogenesis to weaken the tumor nutrient supply.[2] Besides these biomolecules, different nanomedicines, such as a Au_2Pt-PEG-Ce6 nanoformulation (PEG: polyethylene glycol),[25] MCMnH/CaO_2,[26] and ICG@Mn/Cu/Zn-MOF@MnO_2,[27] have been exploited for multimodal imaging-guided synergistic PTT/PDT/CDT. To most effectively treat tumors, it would be beneficial to establish an all-in-one photocatalyst-based bioplatform for cancer therapy *via* PTT/type I and II PDT/CDT to leverage the synergistic effect of multimodal therapy.

Most recently, Schottky junctions prepared by integrating inorganic metals and semiconductors *via* tight contact have demonstrated value for applications including optoelectronics, energy storage, and nanomedicine due to the high photoabsorption ability and superior separation of photoinduced charges.[28−30] However, only a few Schottky junctions such as Ti_3C_2@chitosan-$MnFe_2O_4$[31] and Ag/AgCl NPs[32] have been used as multimodal bioplatforms for antitumor therapy. As an important category of PSs, phthalocyanine (Pc) molecules, with electronic delocalization of 18 electrons, possess distinct and high-efficiency near-infrared (NIR) light absorption, low phototoxicity, and high extinction owing to their highly conjugated planar structures and ability to coordinate with a diversity of metal ions.[33] Various transition metal ions can be coordinated with nitrogen atoms on Pc rings to form metallophthalocyanine (MPc) complexes with M-N_4 structures (e.g., M = Zn, Ni, Fe), which are outstanding active sites for driving photocatalytic reactions, especially type I and II PDT, PTT PSs, or nanozymes.[34,35] In addition, MXenes, two-dimensional (2D) transition metal carbides, carbon nitrides, and nitrides have been extensively utilized as PTT agents in the NIR region for the treatment of different cancers.[36−38] Among MXenes, titanium carbide ($Ti_3C_2T_x$, T = F, O, and OH group) exhibits high photothermal conversion efficiency (PCE) for tumor ablation, thus showing appealing potential for photoinduced cancer therapy.[39] $Ti_3C_2T_x$ MXene[40] and composites such as $Ti_3C_2T_x$-Pt-PEG,[41] 2D Ti_3C_2/g-C_3N_4 heterostructure,[39] Ti_3C_2@chitosan-$MnFe_2O_4$,[31] and CD@$Ti_3C_2T_x$ heterojunctions[42] have demonstrated PTT performance in the NIR I biological window for anticancer therapy.[21,43] On account of the superior photocatalytic ability of Pcs and high photothermal performance of $Ti_3C_2T_x$ MXene, the establishment of the Schottky junctions between MPcs and $Ti_3C_2T_x$ MXene is promising as a multimodal platform between the conjugated CoPc-Mn complex and ultrathin $Ti_3C_2T_x$ nanosheets (NSs). A variety of MXene@Pc junctions have been developed as electrocatalysts or electronics,[44−46] but rarely as nanozymes for tumor therapy. Also, even though some $Ti_3C_2T_x$-based composites or hybrids have been used as multimodal anticancer agents,[47] the combination of type I and type II PDT with PTT and CDT has yet to be realized. Moreover, based on the investigation of the catalytic mechanism of these now-available Schottky junctions, the relative value of each component for multimodal cancer therapy based on the MPcs/$Ti_3C_2T_x$ Schottky junction has yet to be fully characterized.

Herein, we demonstrate a Schottky junction based on a manganese-bridged cobalt−phthalocyanines complex and $Ti_3C_2T_x$ NSs (CoPc-Mn/$Ti_3C_2T_x$) and explore its value as an "all-in-one" photoacoustic imaging-guided PTT/PDT/CDT multimodal therapeutic platform (Scheme 1). The CoPc-Mn complex and $Ti_3C_2T_x$ NSs were assembled through $\pi-\pi$ stacking and hydrogen bonding,[48,49] creating a Schottky junction due to their ultrathin NS-like structure. Further, PEG was used to modify CoPc-Mn/$Ti_3C_2T_x$ (represented as CoPc-Mn/$Ti_3C_2T_x$-PEG) to enhance water solubility and biocompatibility.[50] This Schottky junction substantially enhanced electron−hole separation and exhibited potent redox potential for self-supplying H_2O_2 and O_2. Benefiting from the superior photocatalytic abilities of the two components, the proposed CoPc-Mn/$Ti_3C_2T_x$-PEG Schottky junction not only showed substantially high photothermal performance under NIR light irradiation and outstanding photoacoustic imaging (PAI) capability, but also exhibited synergistic type I PDT and type II PDT performance, resulting in the production of $\cdot O_2^-$, H_2O_2, and ·OH through electron transfer and the generation of $^1O_2$ through energy transfer. The enhanced PCE of the CoPc-Mn/$Ti_3C_2T_x$-PEG Schottky junction stimulated the production of ·OH through Fenton-like reactions of two redox pairs (Co^{2+}/Co^{3+} and Mn^{2+}/Mn^{3+}). Given the good biocompatibility and high stability of the junction in combination with the tumor-targeting ability of the AS1411 aptamer strand, the CoPc-Mn/$Ti_3C_2T_x$-PEG/AS1411 nanozyme demonstrated a high therapeutic efficacy *in vivo*, with an almost complete inhibition of tumor growth. Consequently, the developed MPc/$Ti_3C_2T_x$ Schottky junction is a potential multifunctional nanoplatform for cancer therapy.

RESULTS AND DISCUSSION

Synthesis and Characterizations of the CoPc-Mn/$Ti_3C_2T_x$ Nanozyme. As depicted in Scheme 1, the CoPc-Mn complex was first prepared by the aggregation of CoPc-Mn sheets (Figure S1), and ultrathin $Ti_3C_2T_x$ NSs were obtained by HF etching of Ti_3AlC_2 powders and exfoliation (Figure S2). CoPc-Mn/$Ti_3C_2T_x$ composite was formed by assembly of the CoPc-Mn complex and the exfoliated ultrathin $Ti_3C_2T_x$ NSs *via* $\pi-\pi$ stacking interaction and hydrogen bonds.[48,49] Thus, the CoPc-Mn/$Ti_3C_2T_x$ Schottky junction exhibits a layer-on-layer structure. Field emission scanning electron microscopy (FE-SEM) (Figure S3a and b) and transmission electron microscopy (TEM) (Figure 1a, b, and c) images of CoPc-Mn/$Ti_3C_2T_x$ confirm this finding, suggesting the successful integration of the two components. The TEM and FE-SEM images indicated the average size of the CoPc-Mn/$Ti_3C_2T_x$ composite is about 200

https://doi.org/10.1021/acsnano.2c12270
ACS Nano 2023, 17, 11290−11308

Scheme 1. Schematic illustration of the preparation procedure used to create CoPc-Mn/$Ti_3C_2T_x$-PEG/AS1411 and the *in vivo* PTT/PDT/CDT synergistic antitumor mechanism.

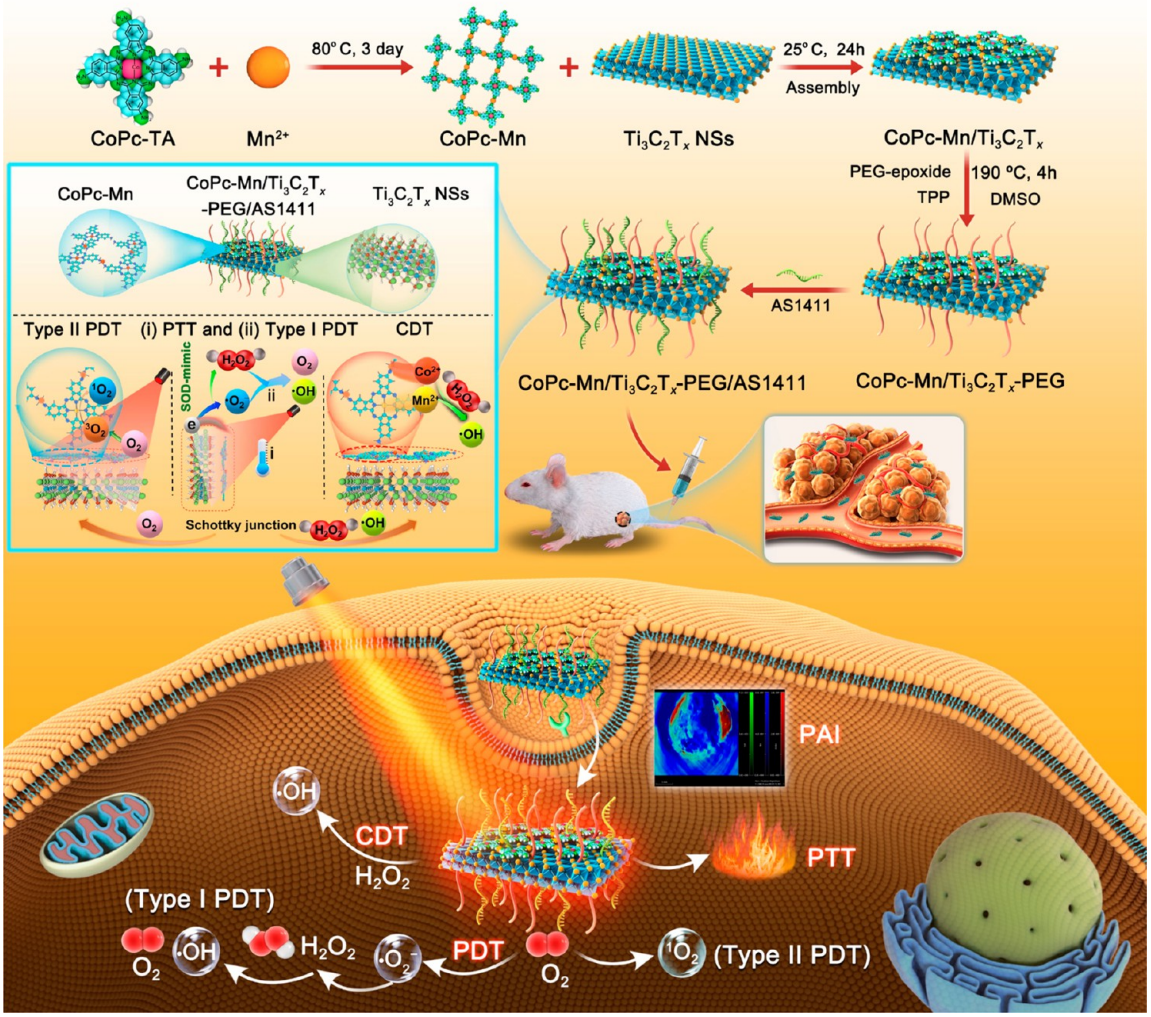

nm. The high-resolution TEM (HR-TEM) image (Figure 1c) exhibits a clear lattice spacing of 0.248 nm, corresponding to the (106) crystal plane of $Ti_3C_2T_x$ NSs (JCPDS 52−0875).[51] The selective-area electron diffractometry (SAED) pattern of CoPc-Mn/$Ti_3C_2T_x$ (Figure 1c, inset) demonstrates a ring pattern, suggesting its low crystallinity. Notably, the high-angle annular dark-field scanning TEM (HAADF-STEM) image of CoPc-Mn/$Ti_3C_2T_x$ shows some bright dots highlighted by yellow circles, which can be attributed to the atomically dispersed M−N sites (Figure 1d). The HAADF-STEM result manifests the homogeneous dispersion of isolated dual single atoms of Co−N and Mn−N in the CoPc-Mn complex, improving the photocatalytic and chemical catalytic abilities and therapeutic efficacy.[52] Moreover, the energy dispersive X-ray spectroscopy (EDS) mapping images of CoPc-Mn/$Ti_3C_2T_x$ (Figure 1e) illustrates that Co, Mn, C, O, and N are homogeneously dispersed in the whole horizon. In contrast, Ti is only present in the $Ti_3C_2T_x$ region. According to the EDS spectrum, the Co, Mn, and Ti atomic % in CoPc-Mn/$Ti_3C_2T_x$ are around 2.45%, 1.57%, and 4.90%, respectively. Moreover, CoPc-Mn/$Ti_3C_2T_x$-PEG (Figure S3c and d) comprises larger particles, revealing the coverage of PEG layer. The further modification of the target aptamer AS1411 exhibits no significant influence on the morphology of CoPc-Mn/$Ti_3C_2T_x$-PEG (Figure S4). Furthermore, the atomic force microscopy (AFM) images (Figure S5) indicate that the thicknesses of the CoPc-Mn complex and $Ti_3C_2T_x$ NSs are 1.5 and 1.5 nm, respectively. After being assembled into a CoPc-Mn/$Ti_3C_2T_x$ Schottky junction, the thickness increased to 3 nm. To further elucidate the layer-on-layer structure of CoPc-Mn/$Ti_3C_2T_x$, the chemical distributions of all ingredients in the CoPc-Mn/$Ti_3C_2T_x$ were investigated using the depth profiling time-of-flight secondary ion mass spectrometry (ToF-SIMS). The primary chemical species in $Ti_3C_2T_x$ NSs layers is Ti^+. Meanwhile, Co^+, Co_2CN^+, and Mn^+ are selected as the dominating chemical species in CoPc-Mn complex layers. As shown in Figure S6, the distributions of Ti^+, Co^+, Co_2CN^+, and Mn^+ are estimated as constant except at the premier pre-equilibrium stage, indicating that the concentration ratio of $Ti^+/Co^+/Mn^+$ remains constant in the *z*-plane.[53] Therefore, $Ti_3C_2T_x$ NSs layers and CoPc-Mn complex layers of CoPc-Mn/$Ti_3C_2T_x$ exhibited a relatively uniform distribution.

The X-ray absorption fine structure spectrum was then collected to determine the local coordination structures of Co and Mn atoms in the CoPc-Mn complex. Representative metallic substances (i.e., Co foil and Mn foil) and MPc-TA (M = Co, Mn) containing Co−N_4 or Mn−N_4 moieties were used as reference samples. The X-ray absorption near-edge

https://doi.org/10.1021/acsnano.2c12270
ACS Nano 2023, 17, 11290−11308

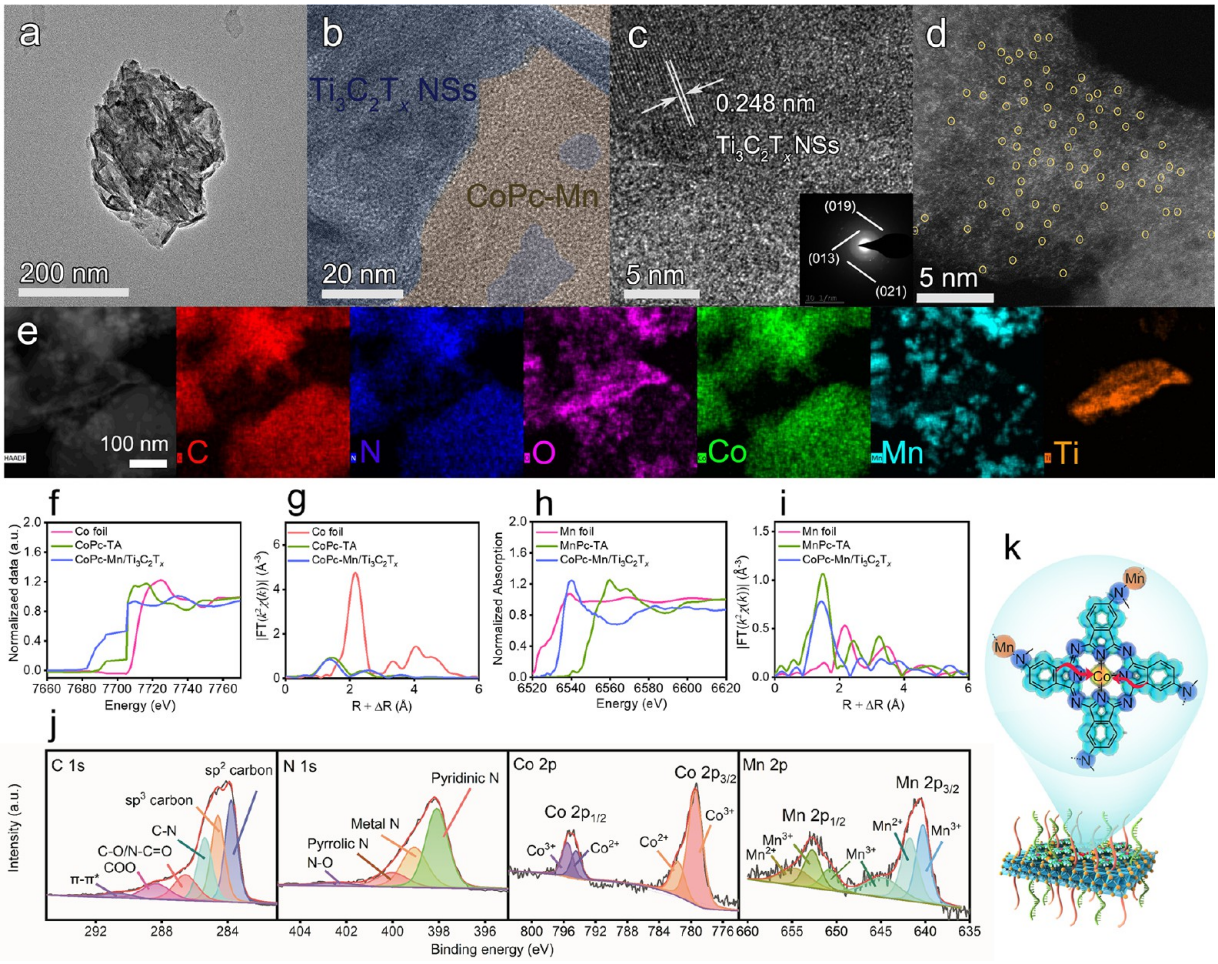

Figure 1. (a, b, and c) Low-magnification, high-magnification, and high-resolution TEM images of CoPc-Mn/$Ti_3C_2T_x$ (inset: SAED pattern of CoPc-Mn/$Ti_3C_2T_x$). (d) HAADF-STEM image of CoPc-Mn/$Ti_3C_2T_x$ and (e) corresponding EDS mapping images of CoPc-Mn/$Ti_3C_2T_x$: C (red), N (blue), O (amaranth), Co (green), Mn (cyan), and Ti (orange). (f) Co K-edge XANES spectra and (g) Fourier-transformed EXAFS spectra of Co foil, CoPc-TA, and CoPc-Mn/$Ti_3C_2T_x$. (h) Mn K-edge XANES spectra and (i) Fourier-transformed EXAFS spectra of Mn foil, MnPc-TA, and CoPc-Mn/$Ti_3C_2T_x$. (j) High-resolution XPS spectra of C 1s, N 1s, Co 2p, and Mn 2p of CoPc-Mn/$Ti_3C_2T_x$. (k) The process of interface charge transfer in CoPc-Mn/$Ti_3C_2T_x$.

structure spectra (XANES; Figure 1f) show the pre-edge feature of cobalt tetraaminophthalocyanine (CoPc-TA) and the CoPc-Mn complex at 7693 eV due to the 1s → 3d transition. Meanwhile, a shoulder peak, i.e., well-resolved double absorption-edge peak at 7709 eV owing to 1s → 4p transition, is observed.[54] The pre-edge absorption of the CoPc-Mn complex is higher than that of CoPc-TA, indicating a high centrosymmetric coordination structure.[55] Next, the structural parameters of the Co−N_4 configuration was obtained through Fourier transform of the extended X-ray absorption fine structure (FT-EXAFS) fitting in *k* and *R* space (Figure S7), in which similar spectra are gained. Co−N and Co−C bonds in the CoPc-Mn complex (Table S1) exhibit the lengths of 1.93 and 2.97 (Å), respectively. The coordination number of Co−N is 4, suggesting the coordination modes of the Co atom in the center of Pc rings. In addition, the edge position of the Mn K-edge indicates that Mn is located between Mn foil and MnPc-TA (Figure 1h), while a peak at 1.44 Å is observed in the Mn FT-EXAFS of the CoPc-Mn complex due to Mn−N (Figure 1i). Notably, the structural parameter of the Mn−N_4 configuration in the CoPc-Mn complex is absent according to the FT-EXAFS. Consequently, Mn^{2+} ions appear to be coordinated with the amino group on CoPc-TA, rather than replacing Co atoms in Pc rings. Additionally, Co−Co and Mn−Mn bonds are not found in CoPc-Mn, further verifying the coexistence of Co−N and Mn−N atomic sites generated in the CoPc-Mn complex. This finding is in line with the above HAADF-STEM result of the CoPc-Mn complex.

The X-ray diffraction (XRD) patterns of the CoPc-Mn complex and CoPc-Mn/$Ti_3C_2T_x$ (Figure S8a) display diffraction peaks at 2θ = 7.54°, 9.45°, 14.24°, 17.42°, 27.17°, and 29.03°, similar to those of CoPc-TA.[56] No significant changes are present between the two samples, suggesting the full overlap of $Ti_3C_2T_x$ NSs with the CoPc-Mn complex. CoPc-Mn/$Ti_3C_2T_x$-PEG (curve *iv*, Figure S8a) demonstrates low and relatively broad peaks, apparently showing an amorphous feature due to the coverage of PEG. A detailed description of the Fourier transform infrared spectroscopy (FT-IR) spectra, ultraviolet visible (UV−vis) absorption in dimethylformamide (DMF), and fluorescence spectra of the CoPc-Mn complex, $Ti_3C_2T_x$ NSs, CoPc-Mn/$Ti_3C_2T_x$, and CoPc-Mn/$Ti_3C_2T_x$-PEG is offered in the Supporting Information (Figure S8b−d). The chemical components of all samples were investigated by X-ray photoelectron spectroscopy (XPS) (Figure S9). The high-resolution C 1s XPS spectra of the CoPc-TA and CoPc-Mn complex (Figure S10a) were composed of bulk sp^2 carbon

https://doi.org/10.1021/acsnano.2c12270
ACS Nano 2023, 17, 11290−11308

(283.7 eV), sp^3 carbon (284.5 eV), C−C (285.3 eV), N−C═O (286.5 eV), and COO (288.6 eV). The presence of sp^2 carbon reveals a highly conjugated structure, whereas C−N emanates from the Pc rings. An additional peak of a $\pi-\pi^*$ moiety (290.6 eV) is observed in CoPc-Mn/$Ti_3C_2T_x$ (Figure 1j) due to the introduction of $Ti_3C_2T_x$ MXene. CoPc-Mn/$Ti_3C_2T_x$-PEG (curve *iii*, Figure S10a) has similar deconvoluted groups but without a $\pi-\pi^*$ moiety, possibly due to the coverage of the PEG layer. Further, the O 1s XPS spectra of the CoPc-TA and CoPc-Mn complex (curves *i* and *ii*, Figure S10b) include an oxygen vacancy (O_v, 530.1 eV), C−O (531.9 eV), and adsorbed O (533.2 eV). The presence of O_v can be further verified by the electron paramagnetic resonance (EPR) spectra of the samples. The electrons or holes can be trapped by O_v sites on the catalyst surface bearing the typical defect states to suppress their recombination.[57] With regard to CoPc-Mn/$Ti_3C_2T_x$ and CoPc-Mn/$Ti_3C_2T_x$-PEG, an additional Ti−O peak (529.9 eV) originating from $Ti_3C_2T_x$ MXene was observed (curves *iii* and *iv*, Figure S10b). The N 1s XPS spectra of the CoPc-TA and CoPc-Mn complex (curves *i* and *ii*, Figure S10c) involve pyridinic N (398.2 eV) and metal−N (M−N; 399.3 eV). Two additional weak peaks of pyrrolic N (400.2 eV) and N−O (402.4 eV) appear in CoPc-Mn/$Ti_3C_2T_x$ (Figure 1j), indicating that the nitrogen-related group of CoPc-TA was weakly oxidized during the combination of the two components. Notably, the position of M−N in CoPc-Mn/$Ti_3C_2T_x$ (398.16 eV) is positively shifted relative to that of the CoPc-Mn complex (398.09 eV), suggesting a decrease in electron density around the metal−N.[58] Further, the Co 2p XPS spectra of all samples comprise the mixed valence states of Co^{3+}/Co^{2+} species (Figures 1j and S10d). In contrast, the Co $2p_{3/2}$ of CoPc-Mn/$Ti_3C_2T_x$ is negatively shifted to 779.2 eV (Figure 1j) relative to that of the CoPc-Mn complex (779.9 eV, curve *ii*, Figure S10d). The integration of the CoPc-Mn complex and $Ti_3C_2T_x$ can drive electron transfer from a nitrogen-related group to Co (Figure 1k). Moreover, the Mn 2p XPS spectra also include the mixed valence states of Mn^{2+}/Mn^{3+} (Figures 1j and S10e).[59] The redox of Mn^{2+}/Mn^{3+} and Co^{2+}/Co^{3+} in the CoPc-Mn/$Ti_3C_2T_x$ can markedly enhance CDT efficiency.[60] Furthermore, the Ti 2p XPS spectra of CoPc-Mn/$Ti_3C_2T_x$ and CoPc-Mn/$Ti_3C_2T_x$-PEG are analyzed in Figure S10f. Two peaks located at 458.2 and 458.8 eV are related to the Ti^{3+} signal and Ti−OH of $Ti_3C_2T_x$ NSs, respectively. In addition, the peak at 464.4 eV corresponds to the Ti−O bond. The Ti−$(OH)_x$ peak area of CoPc-Mn/$Ti_3C_2T_x$-PEG (curve *ii*) was decreased compared with the CoPc-Mn/$Ti_3C_2T_x$ hybrid (curve *i*) due to the reaction of Ti−$(OH)_x$ with PEG-epoxide, indicating the successful modification of PEG. It can further be confirmed by thermogravimetric analysis (TGA) of CoPc-Mn/$Ti_3C_2T_x$-PEG (Figure S8e), with the weight losses of CoPc-Mn/$Ti_3C_2T_x$ and CoPc-Mn/$Ti_3C_2T_x$-PEG as 14.13% and 30.8% at 325 °C, respectively. A detailed description of the FT-IR, XPS, and dynamic light scattering (DLS) spectra of CoPc-Mn/$Ti_3C_2T_x$-PEG/AS1411 is provided in the Supporting Information (Figure S11). This FT-IR and XPS data confirm that AS1411 strands can be efficiently anchored over CoPc-Mn/$Ti_3C_2T_x$-PEG to enhance tumor cell targeting.

Figure S12 shows signals at $g = 1.998$ in the EPR spectra of all samples without or under NIR light irradiation, which can be attributed to defects or element vacancies.[61] It is obvious that CoPc-Mn/$Ti_3C_2T_x$ exhibits a higher g signal intensity, compared with either the CoPc-Mn complex or $Ti_3C_2T_x$ NSs. Accordingly, the defects and vacancies caused by the formation of Schottky junctions at the interfaces between the CoPc-Mn complex and $Ti_3C_2T_x$ NSs can regulate the electronic structure of the CoPc-Mn complex. Notably, the signal at $g = 1.998$ in the CoPc-Mn complex is enhanced by irradiation with NIR laser light (Figure S12). Alternatively, no significant change is observed in the g signal intensity of $Ti_3C_2T_x$ NSs before and after NIR laser irradiation. Further, the g signal in CoPc-Mn/$Ti_3C_2T_x$ is substantially increased under the illumination with an NIR laser, revealing the delocalization of electrons and generation of a greater number of oxygen vacancies. Thereby, the CoPc-Mn/$Ti_3C_2T_x$ Schottky junction is significantly more sensitive for stimulating the generation of defects and vacancies under NIR irradiation than its individual components, boosting its photocatalytic ability. The UV−vis absorption spectra of CoPc-Mn/$Ti_3C_2T_x$ and CoPc-Mn/$Ti_3C_2T_x$-PEG dispersed into DMF (Figure S8c) showed an obvious 12 nm red shift of the Q-band compared to the CoPc-Mn complex due to the strong $\pi-\pi$ interaction between the CoPc-Mn complex and $Ti_3C_2T_x$ NSs, which can reduce the aggregation of the CoPc-Mn complex. Furthermore, CoPc-Mn/$Ti_3C_2T_x$ demonstrated enhanced absorbance in the NIR range, facilitating photothermal conversion. The UV−vis absorption spectra of the catalysts (100 μg mL^{-1}, Figure S13) displayed characteristic peaks at around 808 nm in water, showing an obvious red shift of the Q-band compared to CoPc-Mn/$Ti_3C_2T_x$ in DMF, suggesting their strong potential for photothermal heating when exposed to NIR light in an aqueous environment.

***In Vitro* Photothermal Performance.** Considering the broad absorption of CoPc-Mn/$Ti_3C_2T_x$ tailed up to the NIR region, the photothermal performance of all samples in water is shown in Figures 2 and S14. The temperature increases rapidly for the first 5 min and then slowly approaches an equilibrium (Figure S14a), which is consistent with the corresponding infrared thermal images (Figure S14b). By contrast, no substantial temperature elevation is observed for water under NIR irradiation. These results strongly support the idea that the catalyst is solely responsible for the temperature increase. After irradiation with an 808 nm laser for 10 min, CoPc-Mn/$Ti_3C_2T_x$ achieves a temperature of 68.0 °C, which is higher than that achieved by the CoPc-Mn complex (61.9 °C), but lower than $Ti_3C_2T_x$ NSs (70.2 °C). CoPc-Mn/$Ti_3C_2T_x$-PEG achieves a comparatively lower temperature of 53.6 °C, indicating that the PEG layer marginally weakens photothermal conversion. Notably, CoPc-Mn/$Ti_3C_2T_x$-PEG/AS1411 shows a temperature of 52.6 °C, indicating that AS1411 has a negligible effect on the PTT property of CoPc-Mn/$Ti_3C_2T_x$-PEG/AS1411. Distinctly, the integration of the CoPc-Mn complex and $Ti_3C_2T_x$ NSs can modulate the photothermal property, making the junction favorable as a PTT agent. Furthermore, the CoPc-Mn/$Ti_3C_2T_x$ and CoPc-Mn/$Ti_3C_2T_x$-PEG showed increasingly elevated temperatures at increasing concentrations (Figures S14c and 2b) and irradiation power density (Figures S14e and S15). These findings are in line with corresponding infrared thermal images (Figures S14d, 2c, and S14f). Given that lower dosages of catalyst can potentially decrease side effects, 100 μg mL^{-1} of CoPc-Mn/$Ti_3C_2T_x$ and CoPc-Mn/$Ti_3C_2T_x$-PEG were used in subsequent experiments, achieving temperatures of 68.0 and 53.6 °C (808 nm laser, 1 W cm^{-2}), respectively. According to eqs S1−S6, the PCEs of each sample, η, were determined and used to evaluate their PTT abilities (Figure S16a−e, Figure 2d, and Table S2). Clearly, the CoPc-Mn complex has a smaller η (56.6%, Figure S16b) than that of $Ti_3C_2T_x$ NSs (78.6%, Figure S16c), but higher than those of some Pc-related nanomaterials

https://doi.org/10.1021/acsnano.2c12270
ACS Nano 2023, 17, 11290−11308

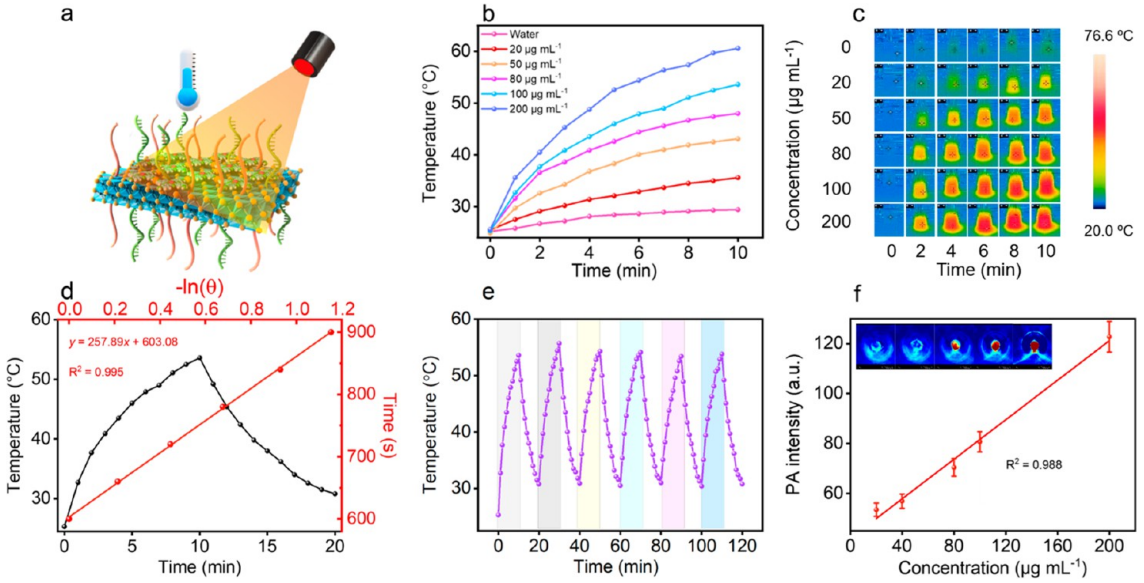

Figure 2. (a) *In vitro* photothermal performance of CoPc-Mn/$Ti_3C_2T_x$-PEG. (b) Temperature elevation curves of CoPc-Mn/$Ti_3C_2T_x$-PEG at various concentrations irradiated with 808 nm laser for 10 min (0−200 μg mL^{-1}). (c) Infrared thermal images of CoPc-Mn/$Ti_3C_2T_x$-PEG aqueous solutions at different concentrations under irradiation with a NIR laser (808 nm) for 10 min. (d) Heating and cooling curves of CoPc-Mn/$Ti_3C_2T_x$-PEG (100 μg mL^{-1}) (black) and the $t-(-\ln\theta)$ diagram obtained during the natural cooling period of CoPc-Mn/$Ti_3C_2T_x$-PEG (red). (e) Photothermal profile of the CoPc-Mn/$Ti_3C_2T_x$-PEG solution over five on/off cycles under 808 nm laser irradiation (100 μg mL^{-1}, 1 W cm^{-2}). (f) *In vitro* PA values of CoPc-Mn/$Ti_3C_2T_x$-PEG at different concentrations (20, 40, 80, 100, and 200 μg mL^{-1}).

such as Pc NPs (31.3%),[62] Pc-based nanodots (ZnPc-NDs) (45.7%),[63] Pc-based polymeric micelles (47.0%),[64] and albumin−iron(II) FePc NPs (HSA-FePc NPs; 44.4%).[65] The η of CoPc-Mn/$Ti_3C_2T_x$ was 66.2% (Figure S16d), falling between the PTT effects of the CoPc-Mn complex and $Ti_3C_2T_x$. Further, comparable η values of CoPc-Mn/$Ti_3C_2T_x$-PEG (63.5%, Figure 2d) and CoPc-Mn/$Ti_3C_2T_x$-PEG/AS1411 (59.8%, Figure S16e) are obtained, suggesting the PEG layer and AS1411 aptamers do not substantially alter the PTT effects. Notably, the PCE of CoPc-Mn/$Ti_3C_2T_x$-PEG/AS1411 outperforms most widely reported photothermal agents such as metallic Mo_2C@N-carbon@PEG NPs (52.7%),[66] MOF-derived composites (29.15%),[67] and $Ni_3S_2/Cu_{1.8}S$ nanoheterostructures (49.5%).[68] After five on−off cycles of NIR laser exposure, the maximum temperatures of CoPc-Mn/$Ti_3C_2T_x$, CoPc-Mn/$Ti_3C_2T_x$-PEG, and CoPc-Mn/$Ti_3C_2T_x$-PEG/AS1411 remain unchanged (Figures 2e and S17a and b), confirming their excellent photostability. Moreover, the photoacoustic signals in aqueous solutions containing different concentrations of CoPc-Mn/$Ti_3C_2T_x$-PEG (Figure 2f) linearly increase with increasing the dosage of CoPc-Mn/$Ti_3C_2T_x$-PEG (R^2 = 0.988), which even can be detected at a low dosage of 20 μg mL^{-1}. This finding suggests that the CoPc-Mn/$Ti_3C_2T_x$-PEG junction has exciting potential as an *in vivo* PAI contrast agent.

Optical and Photoelectrochemical Properties of CoPc-Mn, $Ti_3C_2T_x$ NSs, and CoPc-Mn/$Ti_3C_2T_x$. The UV−vis diffuse reflectance spectroscopy (DRS) spectra of CoPc-Mn/$Ti_3C_2T_x$, the CoPc-Mn complex, and $Ti_3C_2T_x$ NSs (Figure 3a) suggest strong photoabsorption within the NIR region due to the absorption at 200−1000 nm. Further, the photocurrents of all catalysts (Figure 3b) display reversible responses during NIR irradiation. CoPc-Mn complexes as an excellent semiconductor can easily transfer light energy to electrochemical energy, thus generating photocurrent signals.[69] It demonstrates that $Ti_3C_2T_x$ NSs, as cocatalysts, can more efficiently receive photoexcited electrons,[70] which enables improved NIR photocatalytic performance. Therefore, the recombination of photogenerated electrons and holes of CoPc-Mn was efficiently inhibited by the Schottky junction formed between $Ti_3C_2T_x$ NSs and CoPc-Mn.[71] The photocurrent intensity of the CoPc-Mn/$Ti_3C_2T_x$ electrode is higher than the intensities of the CoPc-Mn complex and $Ti_3C_2T_x$ (Figure 3b), revealing its high separation and transfer capability of photogenerated carriers. The photoluminescence (PL) spectrum measurements (Figure 3c) illustrate that the fluorescence intensities of the CoPc-Mn complex and CoPc-Mn/$Ti_3C_2T_x$ significantly decrease at an excitation wavelength of 350 nm relative to $Ti_3C_2T_x$ NSs. Given that a low fluorescence intensity of one catalyst indicates its low recombination rate,[63] the recombination rate of electrons and holes in CoPc-Mn/$Ti_3C_2T_x$ decreases. Consequently, CoPc-Mn/$Ti_3C_2T_x$, which exhibits slow electron−hole recombination, possesses superior photocatalytic activity.

The catalytic mechanism of the Schottky junction nanozyme we have developed was studied by calculating its band structures through UV−vis DRS and ultraviolet photoelectron spectroscopy (UPS) analysis. Figure 3d depicts the energy band gaps (E_g) calculated from eq S7 for the CoPc-Mn complex and CoPc-Mn/$Ti_3C_2T_x$ within the two regions. Given that a catalyst with an E_g lower than 1.53 eV can be excited under NIR light irradiation,[72] the E_g values (Q-band) of the CoPc-Mn complex and CoPc-Mn/$Ti_3C_2T_x$ are 1.50 and 1.52 eV, respectively, and the E_g value of $Ti_3C_2T_x$ NSs is 2.12 eV. The energy band structures of the samples were studied through UPS. Figure 3e shows the calculated work functions (W_F, Φ) of the CoPc-Mn complex, $Ti_3C_2T_x$ NSs, and CoPc-Mn/$Ti_3C_2T_x$ are 3.84, 4.11, and 4.23 eV (vs vac), respectively, after subtracting the excitation energy of He I (21.22 eV). The low binding energy tails (E_{edge}) of the CoPc-Mn complex, $Ti_3C_2T_x$ NSs, and CoPc-Mn/$Ti_3C_2T_x$ are around 1.35, 0.98, and 1.21 eV (vs vac), respectively. Consequently, the Fermi levels (E_F) of the CoPc-Mn complex, $Ti_3C_2T_x$ NSs, and CoPc-Mn/$Ti_3C_2T_x$ are −3.84,

https://doi.org/10.1021/acsnano.2c12270
ACS Nano 2023, 17, 11290−11308

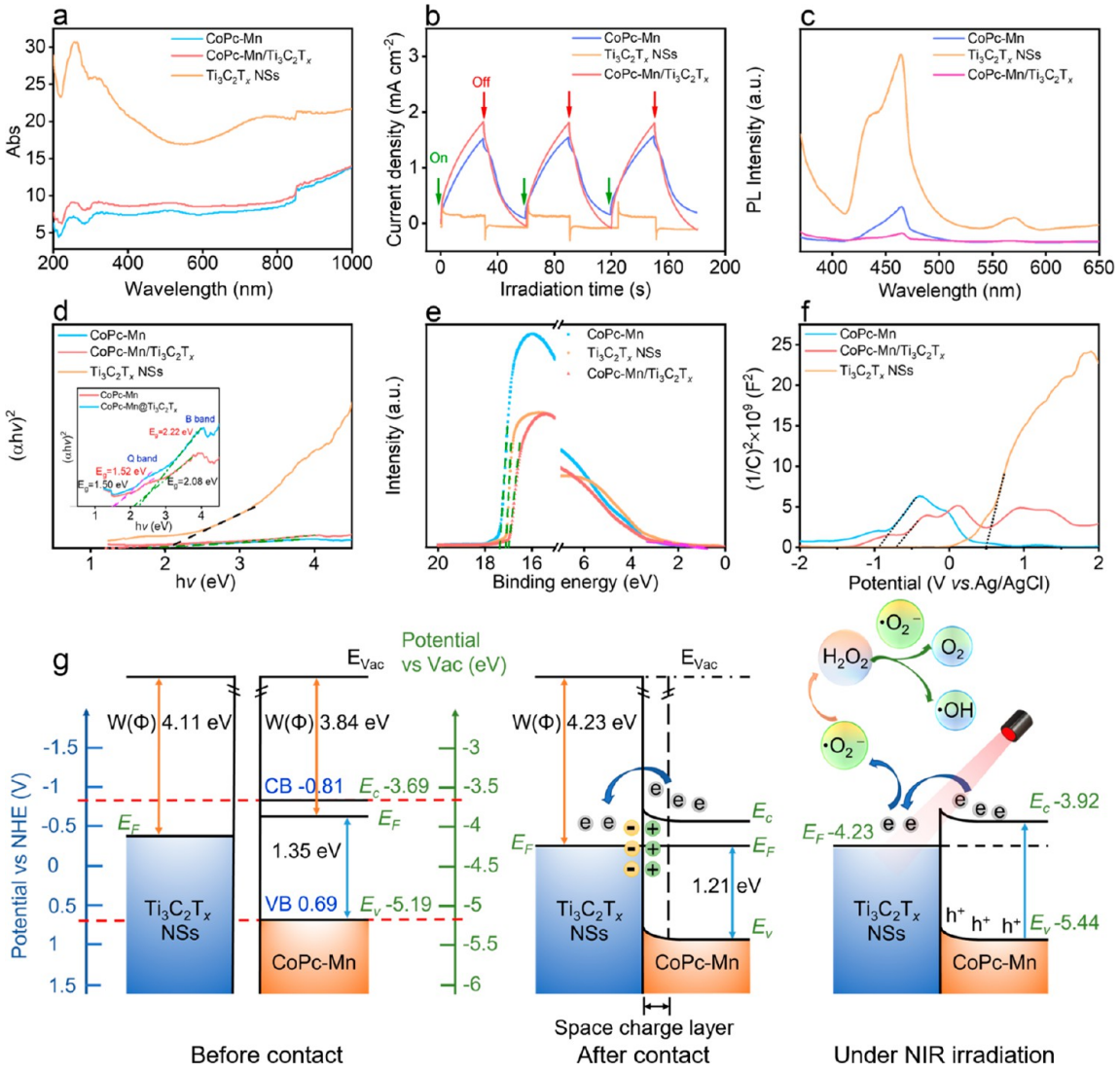

Figure 3. (a) UV−vis DRS absorption spectra, (b) transient photocurrent responses, (c) PL spectra of the CoPc-Mn complex, $Ti_3C_2T_x$ NSs, and CoPc-Mn/$Ti_3C_2T_x$, and (d) the corresponding $[\alpha h\nu]^2$ vs $h\nu$ curves with the inset showing the enlarged sections of CoPc-Mn and CoPc-Mn/$Ti_3C_2T_x$. (e) UPS spectra and (f) M-S plots of the CoPc-Mn complex, $Ti_3C_2T_x$ NSs, and CoPc-Mn/$Ti_3C_2T_x$. (g) Schematic diagram of the change in energy band structure near the interface between $Ti_3C_2T_x$ NSs and the CoPc-Mn complex under different conditions (before contact, after contact, and under NIR irradiation) and the specific process of ROS production during photocatalysis.

−4.11, and −4.23 eV (vs vac), respectively. Given that the E_g of the CoPc-Mn complex and CoPc-Mn/$Ti_3C_2T_x$ are 1.5 and 1.52 eV, respectively, the UPS can be used for the verification of the position of the valence band (VB) according to eqs 1 and 2.[73]

$$E_F - E_V = E_{edge} \quad (1)$$

$$E_C = E_g + E_V \quad (2)$$

Thus, the E_V and conduction band (E_C) of the CoPc-Mn complex are around −5.19 and −3.69 eV (vs vac), respectively, higher than those of CoPc-Mn/$Ti_3C_2T_x$ (E_V = −5.44 eV and E_C = −3.92 eV vs vac). The flat band potentials of the CoPc-Mn complex, $Ti_3C_2T_x$ NSs, and CoPc-Mn/$Ti_3C_2T_x$ are approximately −0.91, 0.50, and −0.71 V (vs Ag/AgCl), respectively, as shown by the Mott−Schottky (M-S) plots in Figure 3f. The CB potentials of the CoPc-Mn complex and CoPc-Mn/$Ti_3C_2T_x$ are −0.81 and −0.61 V (vs NHE, E(vs NHE) = E(vs Ag/AgCl) + 0.197 eV), respectively, which coincide with the results of the UPS curves (−3.69 and −3.92 eV; vs vac). Thereby, the VB top of the CoPc-Mn complex is 0.69 V [vs NHE; −5.19 eV (vs vac)] according to eq 2. Collectively, the schematic illustration of the energy band of CoPc-Mn/$Ti_3C_2T_x$ before and after contact is presented in Figure 3g. The E_F value of the CoPc-Mn complex (−3.84 eV vs vac) is more positive than that of $Ti_3C_2T_x$ NSs; therefore, electrons flow from the CoPc-Mn complex to the $Ti_3C_2T_x$ NS (Figure 3g, before contact). When the CoPc-Mn complex and $Ti_3C_2T_x$ NSs are directly in contact, electrons flow from CoPc-Mn to $Ti_3C_2T_x$ NSs until Fermi equilibrium can be achieved (Figure 3g, after contact). During NIR light irradiation, a positively charged layer on the CoPc-Mn surface is generated owing to the electrons being pumped from VB to CB of the CoPc-Mn complex, resulting in an electron depletion zone and an upward bend in the band edge. Meanwhile, $Ti_3C_2T_x$ NSs, as the cocatalyst and electron sink, accept electrons from the CoPc-Mn complex. Accordingly, a Schottky junction can be generated at the interface between the CoPc-Mn complex and $Ti_3C_2T_x$ NSs, thus gaining appropriate band bending. The Schottky barrier nearly impedes the backflow of electrons, efficiently

https://doi.org/10.1021/acsnano.2c12270
ACS Nano 2023, 17, 11290−11308

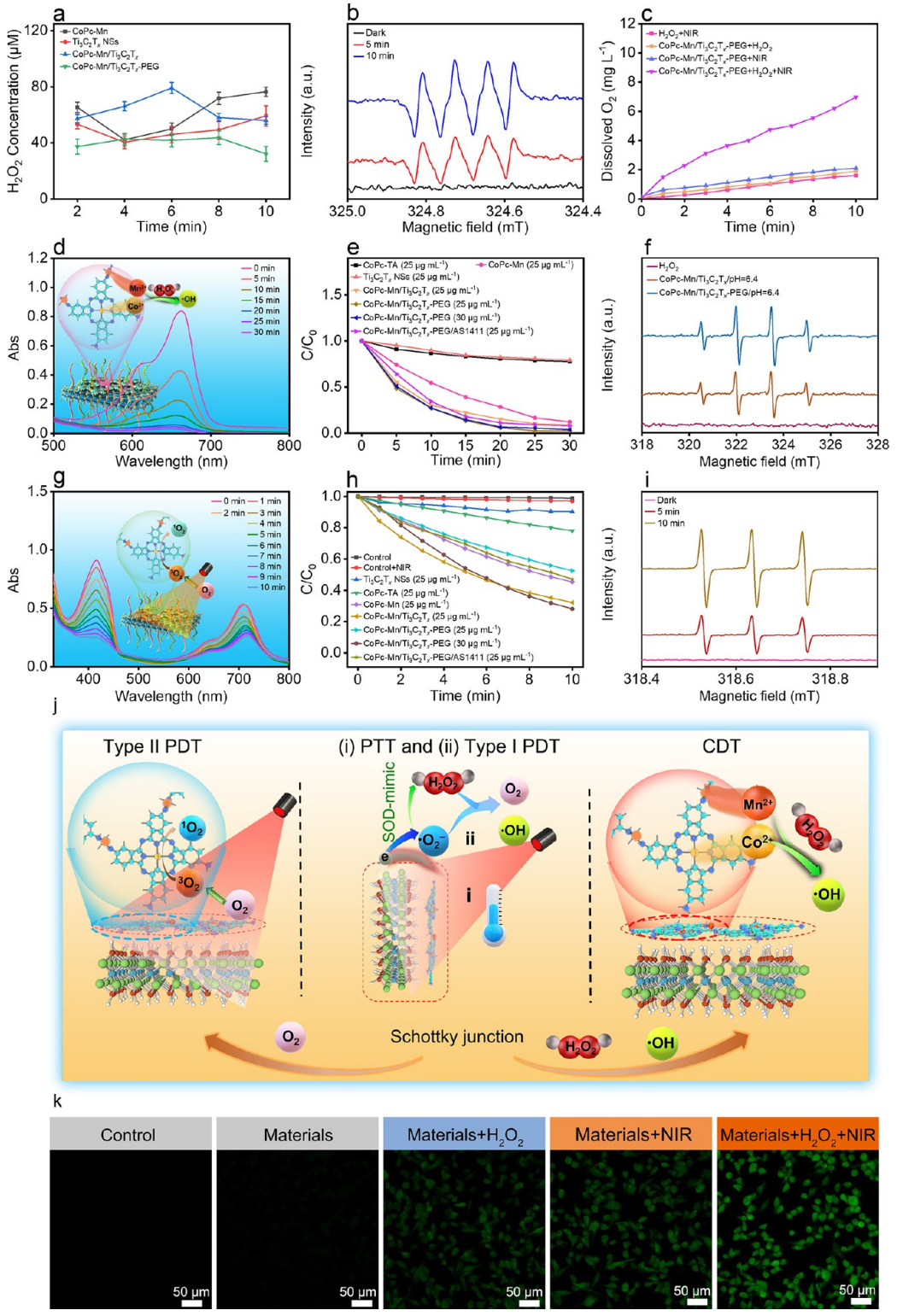

Figure 4. (a) H_2O_2 produced by CoPc-Mn, $Ti_3C_2T_x$ NSs, CoPc-Mn/$Ti_3C_2T_x$, and CoPc-Mn/$Ti_3C_2T_x$-PEG (100 μg mL^{-1}) under 808 nm irradiation for 10 min (1 W cm^{-2}). (b) ESR spectra of CoPc-Mn/$Ti_3C_2T_x$-PEG in the dark and upon 808 nm NIR irradiation for 5 and 10 min in the presence of DMPO-·O_2^-. (c) O_2 generation by CoPc-Mn/$Ti_3C_2T_x$-PEG under differernt conditions. (d) UV−vis absorption spectra of MB caused by CoPc-Mn/$Ti_3C_2T_x$-PEG (30 μg mL^{-1}). (e) Time-dependent degradation of MB caused by CoPc-TA, CoPc-Mn, $Ti_3C_2T_x$ NSs, CoPc-Mn/$Ti_3C_2T_x$, CoPc-Mn/$Ti_3C_2T_x$-PEG, and CoPc-Mn/$Ti_3C_2T_x$-PEG/AS1411. (f) ESR spectra of CoPc-Mn/$Ti_3C_2T_x$ and CoPc-Mn/$Ti_3C_2T_x$-PEG upon the addition of DMPO·. (g) DPBF absorption of the CoPc-Mn/$Ti_3C_2T_x$-PEG (30 μg mL^{-1}) dispersion under 808 nm irradiation (1 W cm^{-2}). (h) Absorbance evolution of DPBF at 417 nm (C/C_0). C_0 is the original absorbance of DPBF, and C is the absorbance of DPBF against irradiation time. (i) ESR spectra of $^1O_2$ trapped by TEMP· in a CoPc-Mn/$Ti_3C_2T_x$-PEG solution with or without 808 nm irradiation (1 W cm^{-2}, 5 and 10 min). (j) Schematic diagram of ROS production process. (k) DCF fluorescence images of DCFH-DA-stained B16 cells treated with CoPc-Mn/$Ti_3C_2T_x$-PEG (100 μg mL^{-1}) at different treatments (materials: CoPc-Mn/$Ti_3C_2T_x$-PEG).

https://doi.org/10.1021/acsnano.2c12270
ACS Nano 2023, 17, 11290−11308

separating the photogenerated electron−hole pairs and increasing the free carrier concentration. As a result, it leads to an electron reservoir of $Ti_3C_2T_x$ NSs, facilitating the separation of photoinduced electrons and holes, prolonging charge carrier lifetime and enhancing CDT and PDT performance.[70]

Generation of ROS and O_2. Based on the previous calculation, the E_{CB} of the CoPc-Mn complex (i.e., −0.81 V vs NHE) is more negative than the reduction potential of $O_2/{\cdot}O_2^-$ (−0.046 V vs NHE), suggesting that $\cdot O_2^-$ could be generated in this system.[74] The corresponding process can be summarized as follows:

$$\text{CoPc-Mn@Ti}_3\text{C}_2\text{T}_x \xrightarrow{h\nu} h^+ + e^- \quad (3)$$

$$O_2 + e^- \rightarrow \cdot O_2^- \quad (4)$$

In fact, CoPc-Mn/$Ti_3C_2T_x$ closely mimics superoxide dismutase (SOD) activity upon NIR light irradiation since it can catalyze the $\cdot O_2^-$ species that are generated into H_2O_2 (eq 5).

$$\cdot O_2^- + 2H^+ + e^- \rightarrow H_2O_2 \quad (5)$$

Based on the standard curve (Figure S18), the concentration of H_2O_2 was determined (Figure 4a). The concentration of the H_2O_2 produced by CoPc-Mn/$Ti_3C_2T_x$ increases during the first 6 min of irradiation, indicating the continuous generation of H_2O_2. After that time, the concentration of H_2O_2 declines, suggesting its consumption. One possible hypothesis is that H_2O_2 can react with $\cdot O_2^-$ and be further converted into ·OH and O_2 *via* the mechanism shown in eq 6.

$$\cdot O_2^- + H_2O_2 \rightarrow \cdot OH + OH^- + O_2 \quad (6)$$

Interestingly, CoPc-Mn/$Ti_3C_2T_x$-PEG exhibits outstanding SOD-mimicking activity. Also, both the CoPc-Mn complex and $Ti_3C_2T_x$ NSs can generate H_2O_2. However, the conversion rate of H_2O_2 to ·OH and O_2 is slower than that of CoPc-Mn/$Ti_3C_2T_x$. To clarify the above mechanism, the category of ROSs produced by catalysts was verified by electron spin resonance (ESR) under an 808 nm laser exposure for 10 min (Figure S19). Figure 4b indicates that the peak intensity of the 5,5-dimethyl-1-pyrroline *N*-oxide (DMPO)-$\cdot O_2^-$ signal increases during irradiation from 5 to 10 min, verifying that $\cdot O_2^-$ species can be produced by catalysis of CoPc-Mn/$Ti_3C_2T_x$-PEG through electron transfer under NIR irradiation. CoPc-Mn/$Ti_3C_2T_x$-PEG shows the strongest ESR signal among all samples, suggesting more $\cdot O_2^-$ is generated *via* the catalysis of CoPc-Mn/$Ti_3C_2T_x$-PEG (Figure S19a). The efficiency of $\cdot O_2^-$ conversion into ·OH and O_2 by reacting with the *in situ*-formed H_2O_2 can be confirmed by the increased DMPO- OH signals produced by CoPc-Mn/$Ti_3C_2T_x$-PEG under NIR irradiation without adding H_2O_2 (Figure S19b). The generated ·OH can also be indirectly shown by determining the concentration of supervenient O_2 in the CoPc-Mn/$Ti_3C_2T_x$-PEG suspension under 808 nm laser irradiation with a dissolved oxygen meter (Figure 4c). Since the dissolved O_2 generated by the *in situ*-formed H_2O_2 is too low to be detected within 10 min, the additional H_2O_2 (100 μM) was added into the CoPc-Mn/$Ti_3C_2T_x$-PEG suspension. As expected, the presence of H_2O_2 in the CoPc-Mn/$Ti_3C_2T_x$-PEG (100 μg mL^{-1}) catalytic systems could generate adequate dissolved O_2 under NIR light irradiation. The above hypothesis is also supported by the photographs of O_2 bubbles in the CoPc-Mn/$Ti_3C_2T_x$-PEG suspension after different treatments (Figure S20). Also, the production of O_2 can be recycled in these bioreactions, facilitate the amelioration of hypoxia, and boost CDT and PDT effects.[75] Accordingly, the production of H_2O_2 can compensate for the intracellular low H_2O_2 level after treatment with CoPc-Mn/$Ti_3C_2T_x$, thereby improving CDT efficacy. CoPc-Mn/$Ti_3C_2T_x$ contains single atomic Co−N_4, Mn−N, and Ti^{3+} active sites and can react with H_2O_2 to generate ·OH according to eqs 7−9.[60]

$$Co^{2+} + H_2O_2 \rightarrow Co^{3+} + \cdot OH + OH^- \quad (7)$$

$$Mn^{2+} + H_2O_2 \rightarrow Mn^{3+} + \cdot OH + OH^- \quad (8)$$

$$Ti^{3+} + H_2O_2 \rightarrow Ti^{4+} + \cdot OH + OH^- \quad (9)$$

To determine the CDT effect of CoPc-Mn/$Ti_3C_2T_x$ and CoPc-Mn/$Ti_3C_2T_x$-PEG, methylene blue (MB) was used as an indicator to capture ·OH radicals. Figures S21b,d−f and 4d illustrate that the absorbance of MB for the CoPc-Mn complex and CoPc-Mn-based catalysts substantially decreases with increasing reaction time in the presence of H_2O_2 because MB is efficiently degraded by ·OH species. No significant degradation of MB could be found in the CoPc-TA + H_2O_2 and $Ti_3C_2T_x$ + H_2O_2 groups (Figure S21a and c), properly caused by the less exposed active sites on the surface. The introduction of Mn ions into CoPc-TA substantially improves the Fenton-like catalytic ability. Figure 4e indicates that the degradation rate of MB against CoPc-Mn/$Ti_3C_2T_x$-PEG (25 μg mL^{-1}) is the highest (97.55%) within 30 min. On the one hand, the enhanced dispersibility of CoPc-Mn/$Ti_3C_2T_x$-PEG provided more catalytic active sites, promoting the CDT performance of CoPc-Mn/$Ti_3C_2T_x$-PEG. On the other hand, the PEGylation of CoPc-Mn/$Ti_3C_2T_x$ resulted in the declination of the effective components (CoPc-Mn/$Ti_3C_2T_x$);[76] the same degradation trend of MB can be obtained when the concentration of CoPc-Mn/$Ti_3C_2T_x$-PEG increased to 30 μg mL^{-1} according to the TGA results. Similar tendencies were also measured in the apparent rate constants (k_a) of the MB degradation (Figure S21g) and ESR measurements (Figure 4f) with the characteristic 1:2:2:1 signal peaks, where the largest k_a value (0.13238 min^{-1}) and sharp peaks' intensity of DMPO-·OH were detected in the presence of CoPc-Mn/$Ti_3C_2T_x$-PEG. These results reflect the outstanding CDT performance of CoPc-Mn/$Ti_3C_2T_x$-PEG. Figure S21i and j show the enhanced Fenton-like activity of CoPc-Mn/$Ti_3C_2T_x$-PEG is the highest (97.55%) in acidic medium (pH 5.4), which is in line with the intensity of peak signals of DMPO-·OH in the ESR spectra of CoPc-Mn/$Ti_3C_2T_x$-PEG with different pH values (Figure S21k).

Herein, we show that CoPc-Mn/$Ti_3C_2T_x$-PEG exhibits excellent photocatalytic abilities under NIR light, generating a spatiotemporally synchronized H_2O_2 and O_2 supply, which overcomes O_2 limitations that typically reduce PDT efficacy. The type II PDT property of all catalysts was measured using 1,3-diphenylisobenzopyran (DPBF) as an indicator. Figure S22a−c show that the pure DPBF and $Ti_3C_2T_x$ NSs + DPBF are not substantially degraded in the dark and with NIR irradiation, suggesting an inferior ability to generate $^1O_2$. However, Figures S22d−h and 4g demonstrate that the DPBF peak intensities against CoPc-TA-based catalysts substantially decrease under NIR irradiation within 10 min, verifying the efficient generation of $^1O_2$. In fact, the PDT effects of the CoPc-Mn complex involve type II PDT as energy transfer occurs.[14] The peak intensity of DPBF against the CoPc-Mn complex is considerably lower than that of CoPc-TA under light irradiation. However, Figure 4h

https://doi.org/10.1021/acsnano.2c12270
ACS Nano 2023, 17, 11290−11308

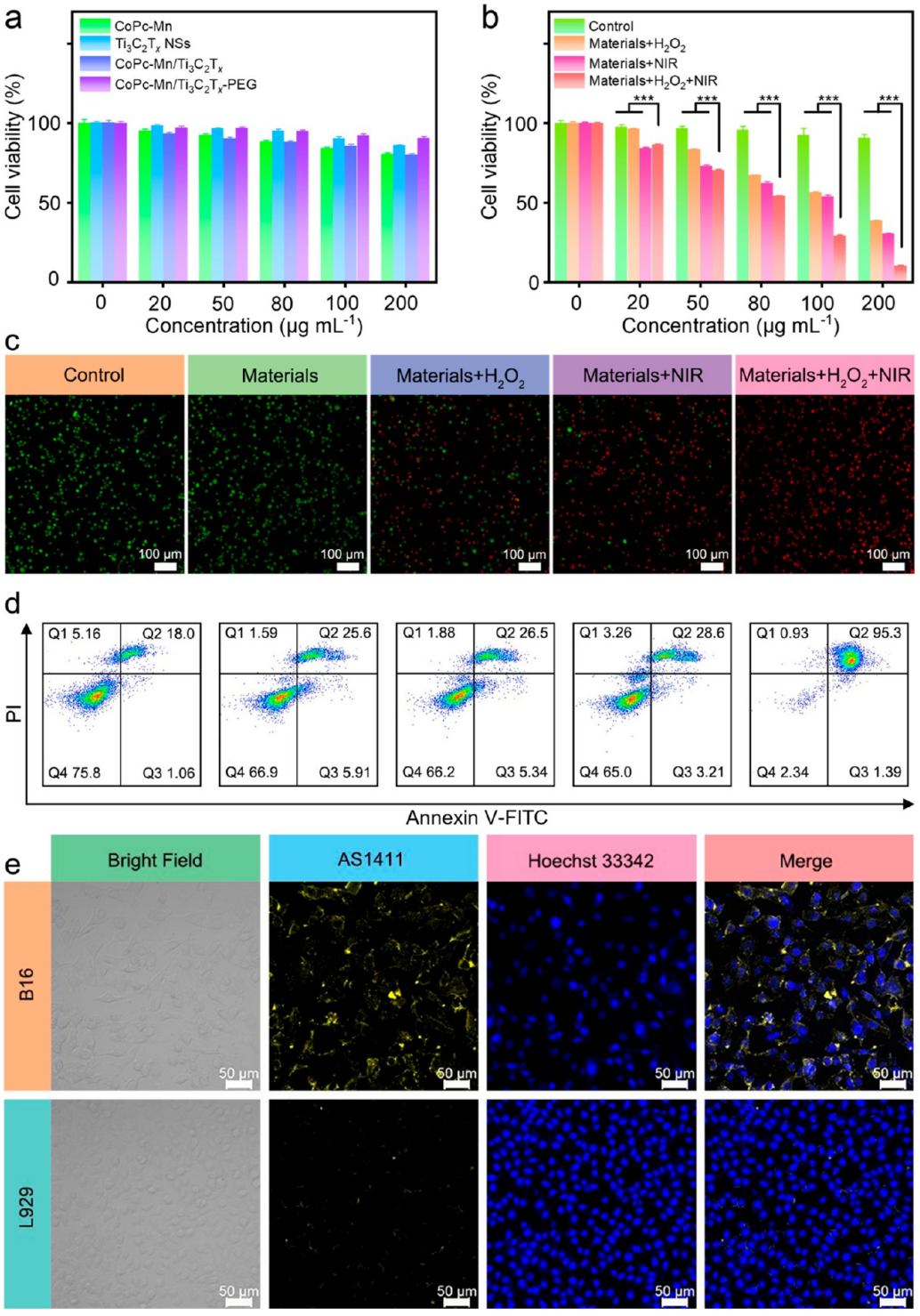

Figure 5. (a) B16 cell uptake and viability when incubated with different concentrations of CoPc-Mn complex, $Ti_3C_2T_x$ NSs, CoPc-Mn/$Ti_3C_2T_x$, and CoPc-Mn/$Ti_3C_2T_x$-PEG (0, 20, 50, 80, 100, and 200 μg mL^{-1}). (b) Cell viabilities of B16 cells treated with different conditions of CoPc-Mn/$Ti_3C_2T_x$-PEG (materials: CoPc-Mn/$Ti_3C_2T_x$-PEG). (c) Fluorescence images of calcein-AM/PI-costained B16 cells under different conditions. (d) Flow cytometry apoptosis assay with B16 cells after different treatments followed by staining with Annexin-FITC and PI. The groups studied included a control, CoPc-Mn/$Ti_3C_2T_x$-PEG, CoPc-Mn/$Ti_3C_2T_x$-PEG + H_2O_2, CoPc-Mn/$Ti_3C_2T_x$-PEG + NIR, and CoPc-Mn/$Ti_3C_2T_x$-PEG + H_2O_2 + NIR. (e) The targeting behaviors of CoPc-Mn/$Ti_3C_2T_x$-PEG/AS1411 in B16 and L929 cells. Data are presented as means ± SD (n = 5). ***P < 0.001.

shows the degradation capacity of CoPc-Mn/$Ti_3C_2T_x$ (67.96%) is higher than that of the CoPc-Mn complex (54.56%) and $Ti_3C_2T_x$ NSs (9.63%), indicating its superior photodegradation activity. This could be ascribed to the Schottky junction of CoPc-Mn/$Ti_3C_2T_x$ NSs, which dramatically boosts PDT efficiency.[39] Additionally, the k_a of DPBF photodegradation of CoPc-Mn/$Ti_3C_2T_x$ is the highest (0.1109 min^{-1}) at the same concentration (Figure S22i and Table S3). However, the degradation capacity and k_a of CoPc-Mn/$Ti_3C_2T_x$-PEG are slightly smaller than those of CoPc-Mn/$Ti_3C_2T_x$, which can

https://doi.org/10.1021/acsnano.2c12270
ACS Nano 2023, 17, 11290−11308

largely be attributed to the cover of some active sites by the PEG layer, hindering the $^1O_2$ generation. To confirm this, the DPBF degradation experiment with the same active component content (30 μg mL^{-1} of CoPc-Mn/$Ti_3C_2T_x$-PEG) was performed according to the TGA results. The similar degradation trends and rates were observed at 25 μg mL^{-1} of CoPc-Mn/$Ti_3C_2T_x$ and 30 μg mL^{-1} of CoPc-Mn/$Ti_3C_2T_x$-PEG (Figure 4g and h). In contrast, the degradation trend (Figure 4h) and k_a of CoPc-Mn/$Ti_3C_2T_x$-PEG/AS1411 (0.0744 min^{-1}) resemble those of CoPc-Mn/$Ti_3C_2T_x$-PEG (0.0630 min^{-1}), which indicates that the AS1411 aptamer has a negligible influence on the PDT performance of CoPc-Mn/$Ti_3C_2T_x$-PEG/AS1411. Collectively, CoPc-Mn/$Ti_3C_2T_x$ can not only promote the generation of $^1O_2$ (type II PDT) through energy transfer but also activate hypoxia-resistant type I PDT by electron transfer under NIR irradiation, which also enhances the synergistic PTT/PDT/CDT effect of CoPc-Mn/$Ti_3C_2T_x$. Also, the generated $^1O_2$ was detected by the ESR during illumination with an 808 nm laser using 2,2,6,6-tetramethylpiperidine (TEMP) as a trapping agent. Three typical characteristic peaks (intensity ratio of 1:1:1) of TEMP-$^1O_2$ were found under NIR light irradiation, while the peak intensity increases along with the irradiation time (Figure 4i). Figure S22j shows obvious TEMP-$^1O_2$ signals of the catalysts containing CoPc-TA under light irradiation, indicating the crucial effect of CoPc-TA components for the production of $^1O_2$.

In accordance with the discussions above, the CoPc-Mn/$Ti_3C_2T_x$ nanozyme-mediated photocatalytic mechanisms that enhance PDT and CDT are proposed (Figure 4j). The formation of a Schottky junction successfully tunes the band of CoPc-Mn/$Ti_3C_2T_x$, benefiting electron−hole separation and transfer, thus exhibiting excellent NIR photocatalytic enhanced therapeutic ability. (i) Type I PDT of CoPc-Mn/$Ti_3C_2T_x$ nanozyme produces $\cdot O_2^-$ by electron transfer under the NIR 808 nm laser irradiation. (ii) The generated $\cdot O_2^-$ species was further converted to H_2O_2 due to the SOD-mimicking activity of CoPc-Mn/$Ti_3C_2T_x$ upon NIR light irradiation and further converted H_2O_2 to ·OH and O_2. (iii) This self-supplying H_2O_2 and O_2 ability of the CoPc-Mn/$Ti_3C_2T_x$ nanozyme can compensate the intracellular H_2O_2 level for enhanced CDT efficacy and alleviate the tumor hypoxia to improve the oxygen-dependent type II PDT efficiency. By integrating type I and type II PDT into one nanoplatform, the effective PDT efficiency can be guaranteed. The superior PCE of $Ti_3C_2T_x$ NSs can be utilized as PTT agents for effective photoacoustic-imaging guided therapy.[39] Such a Schottky junction-associated PDT/CDT enhancement effect can greatly enhance the therapeutic efficacy *via* the synergy between PTT, CDT, and PDT.

Intracellular ROS generation was performed in mouse melanoma B16 cells using 2′,7′-dichlorodiacetate (DCFH-DA), which can be oxidized by ROS to generate green fluorescent 2,7-dichlorofluorescein, as a fluorescent probe (Figure 4k). No green fluorescence was observed in the control and CoPc-Mn/$Ti_3C_2T_x$-PEG groups without NIR irradiation. The CoPc-Mn/$Ti_3C_2T_x$-PEG + H_2O_2 group exhibits weak green fluorescence, suggesting minimal production of ·OH, which is mainly attributed to the Fenton-like reaction mediated by Co-N_4 and Mn-N active sites containing in the CoPc-Mn complex. The group of CoPc-Mn/$Ti_3C_2T_x$-PEG + NIR also shows a weak green fluorescence signal, which can be attributed to ROS generated *via* the PDT effect. By contrast, a strong green fluorescence signal distinctly appears in the CoPc-Mn/$Ti_3C_2T_x$-PEG + H_2O_2 + NIR group, demonstrating increased production of ROSs by promoted CDT and PDT effects.

***In Vitro* Cytotoxicity.** The cytotoxicity of CoPc-Mn/$Ti_3C_2T_x$-PEG was first accessed by the metal ions leaking experiment under different pH values (Figure S23). The results showed that Co ions were hardly released due to its stable Co-N_4 structure formed with Pc. A similar results was observed for Ti ions, which was ascribed to the strong bond between the Ti atom and C atom in $Ti_3C_2T_x$ NSs. Notably, Mn as an essential trace element for the human body exhibited a pH-dependent leaking behavior with a fast release of over 70% of Mn within 4 h at pH 5.5, while less than 35% Mn was released at pH 7.4 within 48 h. The biocompatibility of all samples was further assessed in L929 and B16 cells at 24 and 48 h using the 3-[4,5-dimethylthiazol-2-y1]-2,5-diphenyltetrazolium bromide (MTT) assay. Figure S24a shows that the survival rate of L929 cells treated with CoPc-Mn/$Ti_3C_2T_x$-PEG (200 μg mL^{-1}) was the highest (90.8%), suggesting reduced cytotoxicity under 24 h. Likewise, the CoPc-Mn/$Ti_3C_2T_x$-PEG (200 μg mL^{-1}) group shows a higher survival rate (90%) than that of the CoPc-Mn complex (80.7%) toward B16 cells under 24 h (Figure 5a). As a comparison, the survival rates of B16 cells and L929 cells at high concentrations (100 and 200 μg mL^{-1}) decreased at 48 h, indicating the increased cytotoxicity against concentration. Besides, the survival rate for the CoPc-Mn/$Ti_3C_2T_x$-PEG (200 μg mL^{-1}) group was higher that of the CoPc-Mn/$Ti_3C_2T_x$ group, indicating the enhanced biocompatibility upon PEGylation. The cytotoxicity of CoPc-Mn/$Ti_3C_2T_x$-PEG treated by single- or multitreatment strategies was assessed *in vitro* to differentiate the contributions. Figure 5b indicates that the cell viability of B16 cells declines with increasing the concentration of CoPc-Mn/$Ti_3C_2T_x$-PEG treated by different methods, as expected. The cell viability of B16 cells for the CoPc-Mn/$Ti_3C_2T_x$-PEG + NIR and CoPc-Mn/$Ti_3C_2T_x$-PEG + H_2O_2 groups is 30.5% and 38.6%, respectively, at a CoPc-Mn/$Ti_3C_2T_x$-PEG dosage of 200 μg mL^{-1}, whereas the cell viability of the CoPc-Mn/$Ti_3C_2T_x$-PEG + NIR + H_2O_2 group is around 10.3% because of the multimodal synergistic therapeutic effects.

A LIVE/DEAD stain was used for further confirmation by a calcein AM/PI assay through confocal laser scanning microscopy (CLSM) (Figure 5c) and a flow cytometry assay (Figure 5d). Figure 5c reveals strong red fluorescence for the NIR-treated CoPc-Mn/$Ti_3C_2T_x$-PEG + H_2O_2 group, representing dead cells. However, the experimental groups without laser irradiation or H_2O_2 resulted in few dead cells, which is consistent with MTT results. Figure 5d shows B16 cell apoptosis and necrosis, as evaluated by flow cytometry. After being subjected to different conditions, the NIR-treated CoPc-Mn/$Ti_3C_2T_x$-PEG + H_2O_2 group resulted in the largest percentage of apoptotic cells (95.3%), demonstrating the excellent therapeutic effects of combining PDT, CDT, and PTT. Further, L929 and B16 cells were incubated with the CoPc-Mn/$Ti_3C_2T_x$-PEG/AS1411 to evaluate the targeting capability of nanozymes, and cellular uptake efficiency was monitored by measuring the intracellular fluorescence of 5′-Cy3-labeled AS1411 with CLSM. Figure 5e shows the yellow fluorescence signal in B16 cells compared with the weak fluorescence signal in L929 cells, suggesting the successful endocytosis of B16 cells toward CoPc-Mn/$Ti_3C_2T_x$-PEG/AS1411 through active targeting. As shown in Figure S25, the cellular uptake efficiency of CoPc-Mn/$Ti_3C_2T_x$-PEG/AS1411 calculated by intracellular Co and Ti ions reached the maximum at 4 and 2 h, corresponding to 42.6%

https://doi.org/10.1021/acsnano.2c12270
ACS Nano 2023, 17, 11290−11308

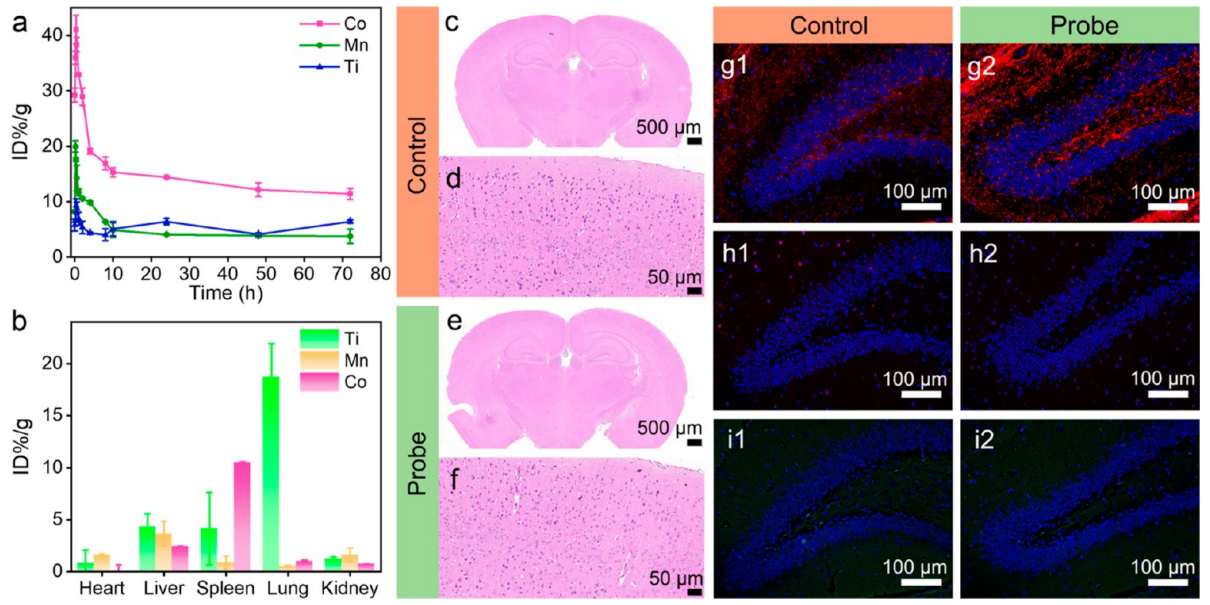

Figure 6. (a) *In vivo* blood circulation and (b) biodistributions of the CoPc-Mn/$Ti_3C_2T_x$-PEG/AS1411 in BALB/c mice, determined by the Ti, Mn, and Co element concentrations in tissue lysates. Data are means ± SD (n = 4). (c–f) H&E staining and immunofluorescent staining images of (g1, g2) MBP (red), (h1, h2) S100β (red), and (i1, i2) FJB (green) of the cortex for the control and CoPc-Mn/$Ti_3C_2T_x$-PEG/AS1411-treated groups, respectively (DAPI: blue).

and 19.4%, respectively. Notably, the Ti ion content declines after culturing 2 h, indicating the exocytosis of Ti ions.

***In Vivo* Biocompatibility Evaluation.** The hematology studies were conducted to access the *in vivo* biocompatibility of CoPc-Mn/$Ti_3C_2T_x$-PEG/AS1411 probe at doses of 0.1, 0.2, and 0.4 mg mL^{-1} in healthy female BABL/c mice (n = 4). After intravenous injection of CoPc-Mn/$Ti_3C_2T_x$-PEG/AS1411 for 14 days, the blood was collected for hematological analysis. The hematology and blood biochemical assay results (Figure S26) indicated there is no abnormal up- or down-regulation of all these blood indexes in concordance with the control group. Additionally, the negligible differences in major liver function indicators, including total bilirubin (TBIL), aspartate aminotransferase (AST), alanine aminotransferase (ALT), γ-glutamyl transferase (γ-GT), and renal function indicators (such as uric acid (UA), creatinine (CREA), and blood urea nitrogen (BUN)), were revealed in both experimental and control groups. All of the above blood analysis results suggest that the CoPc-Mn/$Ti_3C_2T_x$-PEG/AS1411 nanoenzyme at the doses studied would not impact the health status of the mice, thereby ensuring the high biosafety feature for therapeutic applications.

In vivo blood circulation and biodistribution of CoPc-Mn/$Ti_3C_2T_x$-PEG/AS1411 were further disclosed with healthy mice. The levels of metal ions (Co, Mn, and Ti) in major organs and blood samples were determined by inductively coupled plasma mass spectrometry (ICP-MS) measurement after being solubilized in a HNO_3/HCl (v/v: 1/3) solution (Figure 6a). The *in vivo* circulating half-life ($\tau_{1/2}$) of CoPc-Mn/$Ti_3C_2T_x$-PEG/AS1411 in the bloodstream was determined using a double-compartment pharmacokinetic model. The Co and Ti ions exhibited a $\tau_{1/2}$ of 3.48 and 3.38 h, respectively, while Mn ions illustrate a longer half-life time of 7.24 h. Therefore, their long blood circulating time was favorable for the active targeting of CoPc-Mn/$Ti_3C_2T_x$-PEG/AS1411 composites to the tumor sites by blood circulation. The prolonged half-life time of Mn ions indicates their escape from the immune system, followed by metabolism in blood circulation. In fact, low levels of Mn element (0.5–3.6%ID/g) were observed in the major organs 14 days postinjection (Figure 6b). Notably, a high level of Ti element was observed in major organs (liver, spleen, lung, and kidney), suggesting the uptake of the CoPc-Mn/$Ti_3C_2T_x$-PEG/AS1411 by the mononuclear phagocyte system. Different from the fate of Ti element, a higher content of Co element was detected in the spleen than that of the liver and kidney, indicating the different fates *in vivo*.

For the long-term cytotoxicity of CoPc-Mn/$Ti_3C_2T_x$-PEG/AS1411 to the central nervous system, the brain tissues of mice were extracted 30 days postinjection for histological and immunohistochemical analysis. Hematoxylin and eosin (H&E) staining images (Figure 6c–f) show that the nerve cells in the cortex are densely organized with a regular morphology, and the nuclei are large and round with clear nucleoli, indicating no obvious chronic inflammation in the central nervous system. Myelin basic protein (MBP) and S100β are used as cell markers to assess the damage to the nervous system.[77] Based on the immunofluorescence images of MBP and S100β (Figure 6g and h), the expressions of MBP and S100β in the CoPc-Mn/$Ti_3C_2T_x$-PEG/AS1411-treated group are close to that of the control group. The number of degenerative neurons in the treatment and the control groups can be obtained from the Fluoro-Jade B (FJB) staining.[78] Obviously, insignificant differences of FJB-positive cells in the CoPc-Mn/$Ti_3C_2T_x$-PEG/AS1411-treated and control groups were observed (Figure 6i). These results indicated that the developed CoPc-Mn/$Ti_3C_2T_x$-PEG/AS1411 nanozyme shows a negligible influence on the central nervous system.

***In Vivo* PAI.** The *in vivo* performance of CoPc-Mn/$Ti_3C_2T_x$-PEG/AS1411 as a PAI agent was assessed in a B16-tumor-bearing mice model. Images of the tumor sites were obtained at various times after intravenous injection (Figure 7a and b). Two hours after injection, the PA signal at the tumor sites had clearly increased, indicating the accumulation of PAI agent in the tumor site. After 3 h, the PA signal intensity reached a maximum and then decreased. CoPc-Mn/$Ti_3C_2T_x$-PEG/AS1411 showed

https://doi.org/10.1021/acsnano.2c12270
ACS Nano 2023, 17, 11290–11308

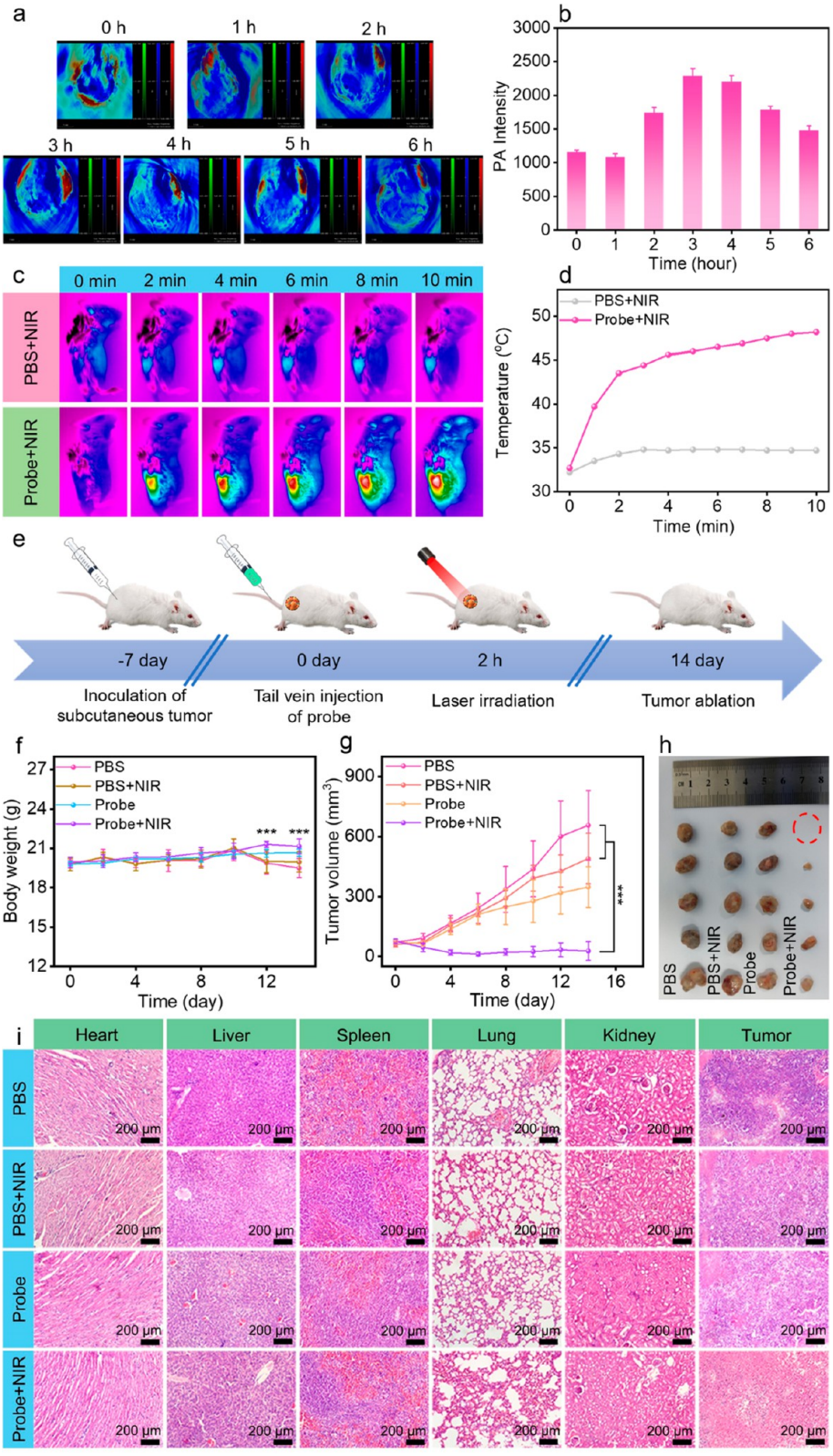

Figure 7. ***In vivo*** **PAI performances and synergistic PTT/PDT/CDT therapeutic efficacy of CoPc-Mn/$Ti_3C_2T_x$-PEG/AS1411 as a probe against B16-tumor-bearing mice. (a) Time-dependent PA images of B16-tumor-bearing mice after postinjection of CoPc-Mn/$Ti_3C_2T_x$-PEG/AS1411 at various time points. (b) The evolution of PA signal intensity as the function of time postinjection. (c) IR thermal images and (d) tumor temperature changes of B16-tumor-bearing mice injected with PBS (as a control) and CoPc-Mn/$Ti_3C_2T_x$-PEG/AS1411 followed by irradiating with an 808 nm NIR laser (1.0 W cm^{-2}, 10 min). (e) Time schedule of CoPc-Mn/$Ti_3C_2T_x$-PEG/AS1411 administration for antitumor therapy. (f) Body weight and (g) tumor volume growth curves of mice after different treatments. (h) Photographs of tumors collected after the whole treatment regimen had been delivered to each group (red circle indicates the completely ablated tumor). (i) H&E histological staining of the main organs and tumor tissues from different treatment groups. Data are means ± SD (n = 5). ***P < 0.001.**

https://doi.org/10.1021/acsnano.2c12270
ACS Nano 2023, 17, 11290−11308

robust accumulation in tumors, demonstrating its potential for PAI-guided cancer therapy. The *in vivo* PA images demonstrate similar trends for oxyhemoglobin and hemoglobin signal intensities around the tumor vasculature, verifying oxygen generation and the alleviation of hypoxia within the tumor site. These collective results indicate that CoPc-Mn/$Ti_3C_2T_x$-PEG/AS1411 can be adopted as a PAI and PTT/PDT agent. Two hours after injection, tumor sites were irradiated with an 808 nm laser for 10 min (1.0 W cm^{-2}), and the temperature of each tumor site was monitored longitudinally during irradiation (Figure 7c and d). Compared with the control groups (treated with PBS and an 808 nm laser), the CoPc-Mn/$Ti_3C_2T_x$-PEG/AS1411-treated group showed substantial temperature elevation. The maximum temperature at the tumor site reached 48.2 °C, leading to tumor cell apoptosis.

***In Vivo* Antitumor Treatment Study.** The *in vivo* synergistic PTT/PDT/CDT therapeutic efficacy under 808 nm laser irradiation was further assessed on a B16-tumor-bearing mice model *via* the tail vein injection of CoPc-Mn/$Ti_3C_2T_x$-PEG/AS1411 with a consecutive treatment process for 14 days with CoPc-Mn/$Ti_3C_2T_x$-PEG/AS1411 or CoPc-Mn/$Ti_3C_2T_x$-PEG/AS1411 + NIR light irradiation 2 h after injection. The average body weight in the control groups slightly declined after 10 days of treatment, whereas the weights for the CoPc-Mn/$Ti_3C_2T_x$-PEG/AS1411-treated group increased, indicating the outstanding biocompatibility of CoPc-Mn/$Ti_3C_2T_x$-PEG/AS1411 (Figure 7f). After 14 days of treatment (Figure 7g), the tumor volume in the group receiving NIR light rapidly grew, suggesting that laser irradiation alone was unable to achieve a complete response. Mice treated with CoPc-Mn/$Ti_3C_2T_x$-PEG/AS1411 without laser irradiation demonstrated a moderate tumor suppression effect, showing a tumor growth inhibition (TGI) rate of 47.1%. This result indicates that the CDT effect of CoPc-Mn/$Ti_3C_2T_x$-PEG/AS1411 is insufficient to inhibit tumor growth in the TME. Apparently, tumor suppression can be achieved for the CoPc-Mn/$Ti_3C_2T_x$-PEG/AS1411 + NIR light group, showing a TGI rate of 95.8%. This therapeutic effect can be attributed to the type I/II-combined PDT, Co^{2+}/Mn^{2+}-mediated CDT, and the PTT effect of CoPc-Mn/$Ti_3C_2T_x$-PEG/AS1411. The photographs of tumor tissues at day 14 are consistent with the tumor growth trend. Tumor size decreased with increasing therapeutic time in the CoPc-Mn/$Ti_3C_2T_x$-PEG/AS1411 + NIR light groups. The tumor in one mouse was completely ablated in the PTT/PDT/CDT-treated group (Figure 7h). Main organs and tumors were harvested after treatment and stained with H&E, and no obvious damage and metastases were found (Figure 7i). Tumor cells were largely eliminated by synergistic PTT/PDT/CDT treatment. TUNEL staining for the tumor tissue confirmed enhanced apoptosis and tumor cell death after PTT/PDT/CDT treatment (Figure S27). Accordingly, the excellent therapeutic performance can be ascribed to the high efficiency of CoPc-Mn/$Ti_3C_2T_x$/AS1411-mediated synergistic PTT/PDT/CDT therapy.

CONCLUSIONS

In summary, a Schottky junction nanozyme was constructed at the interface between the CoPc-Mn complex and $Ti_3C_2T_x$ NSs for efficient tumor treatment through PAI-guided PDT/CDT/PTT therapy. The Schottky junction exhibited a PTT-enhanced CDT/PDT effect because of the efficient CDT effect of the Co^{2+}/Co^{3+} and Mn^{2+}/Mn^{3+} redox-active atomic Co−N and Mn−N sites of the CoPc-Mn complex. The enhanced photoinduced charge separation efficiency was caused by the Schottky barrier junction and high PCE of $Ti_3C_2T_x$ NSs. The integration of type I and II PDT effects and the self-supplying H_2O_2 and O_2 ability were realized. Consequently, the CoPc-Mn/$Ti_3C_2T_x$-PEG-mediated treatment resulted in synergistic cytotoxicity and triggered B16 cell apoptosis. Moreover, the outstanding tumor-targeting accumulation of PAI-agents, excellent biocompatibility of CoPc-Mn/$Ti_3C_2T_x$-PEG/AS1411, and effective tumor inhibition were achieved by the synergistic PDT/PTT/CDT in solid-tumor-bearing mice. This work can facilitate the exploration of the Schottky barrier junction and its application as a multifunctional nanoplatform for the synergistic antitumor therapy against solid tumors.

METHODS

Preparation of $Ti_3C_2T_x$ NSs. Herein, 2D $Ti_3C_2T_x$ NSs were prepared according to a previously published method.[41] Typically, LiF (0.6 g) was dissolved in HCl (10 mL, 12 M). Afterward, Ti_3AlC_2 powders (0.8 g) were added in the LiF solution under the vigorous stirring at 0 °C after 30 min and kept at 40 °C for another 24 h. Subsequently, the mixture was sonicated for 1 h, followed by adding 25 mL of HCl (12 M) to the obtained solution under vigorous stirring for 40 min at 25 °C. After that, the acidic mixture was rinsed using Milli-Q water *via* centrifugal separation for multiple cycles until a pH of 7 was accomplished. A well-dispersed claylike solid suspension (aqueous solution) was gained *via* bath sonication for 2 h. Finally, $Ti_3C_2T_x$ NSs were obtained after centrifugation at 4000 rpm.

Preparation of the CoPc-Mn Complex and the CoPc-Mn/$Ti_3C_2T_x$ Nanozymes. CoPc-TA was synthesized according to the previous work.[56] Afterward, the CoPc-TA suspension (63 mg, 0.1 mmol) was dispersed in Milli-Q water (4 mL), forming a homogeneous suspension. After that, $Mn(NO_3)_2{\cdot}6H_2O$ (14.35 mg, 0.05 mmol) was added into the mixed solvent containing trimethylamine (28 μL) and acetonitrile (2 mL) under thorough stirring at 80 °C for 4 days. Subsequently, the above suspension was centrifuged and rinsed thrice with Milli-Q water. After drying under vacuum at 60 °C, a dark green powder (denoted as the CoPc-Mn complex) was obtained. In this case, Mn^{2+} ions were coordinated with abundant amino moieties on CoPc-TA to yield the CoPc-Mn complex.

In addition, a CoPc-Mn/$Ti_3C_2T_x$ hybrid was prepared by adding exfoliated $Ti_3C_2T_x$ NSs (10 mg) into the CoPc-Mn suspension (1.6 mM, 20 mL) and stirred for 24 h. Subsequently, the CoPc-Mn/$Ti_3C_2T_x$ was post-treated using a method resembling that of the CoPc-Mn complex. Owing to $\pi-\pi$ stacking[49] and hydrogen bonding[48] between the conjugated CoPc-Mn complex and ultrathin $Ti_3C_2T_x$ NSs, the two components can be closely assembled together.

Preparation of CoPc-Mn/$Ti_3C_2T_x$-PEG and CoPc-Mn/$Ti_3C_2T_x$-PEG/AS1411. To improve dispersion and biocompatibility, CoPc-Mn/$Ti_3C_2T_x$ PEGylation was carried out according to the previous literature.[79] Typically, CoPc-Mn/$Ti_3C_2T_x$ (50 mg), PEG-epoxide (500 mg), and triphenylphosphine (12.5 mg) were dispersed in dimethyl sulfoxide (DMSO, 20 mL) and thoroughly stirred until the suspension became transparent. Afterward, the mixture reacted at 190 °C for 4 h under stirring. Finally, the resulting product was obtained by precipitating and rinsing thrice with cold diethyl ether. After drying under vacuum, a CoPc-Mn/$Ti_3C_2T_x$-PEG hybrid was obtained.

In addition, the CoPc-Mn/$Ti_3C_2T_x$-PEG/AS1411 hybrid was prepared by incubating CoPc-Mn/$Ti_3C_2T_x$-PEG with the aptamer AS1411 solution (1 mL, 3 μM) at 4 °C for 2 h. The obtained suspension was treated by centrifugal separation and then washed with PBS thrice to remove the unabsorbed AS1411 strands. Due to the highly conjugated nanostructure and rich amino group of CoPc-Mn/$Ti_3C_2T_x$-PEG, AS1411 strands were immobilized over CoPc-Mn/$Ti_3C_2T_x$-PEG *via* $\pi-\pi$ stacking and electrostatic interaction. The resulting CoPc-Mn/$Ti_3C_2T_x$-PEG/AS1411 was stored in a refrigerator (4 °C) for further experimentation.

***In Vitro* Photothermal Effect.** Different concentrations of CoPc-Mn/$Ti_3C_2T_x$-PEG suspensions (0, 20, 50, 80, 100, and 200 μg mL^{-1})

https://doi.org/10.1021/acsnano.2c12270
ACS Nano 2023, 17, 11290−11308

and CoPc-Mn, $Ti_3C_2T_x$ NSs, CoPc-Mn/$Ti_3C_2T_x$, and CoPc-Mn/$Ti_3C_2T_x$-PEG/AS1411 suspensions (100 μg mL^{-1}) were prepared separately and treated with an NIR 808 nm laser for 10 min. The heat distribution and the system temperature were recorded using a thermal imaging camera and electronic thermometer, respectively, to test the photothermal performance. Different power densities (0.3, 0.65, and 1 W cm^{-2}) of the laser light were also adopted to modulate the temperature.

SOD-Mimicking Catalytic H_2O_2 Production. The obtained catalyst suspension (2 mL, 100 μg mL^{-1}) was transferred to a 4 mL centrifuge tube and subjected to a NIR 808 nm laser light for 0, 2, 4, 6, 8, or 10 min, followed by eliminating the catalyst *via* a 0.22 μm filter. These filtrates were mixed with a $Ce(SO_4)_2$ solution (2 mmol L^{-1}, 200 μL). The yellow solution became colorless when Ce^{4+} ions were reacted with H_2O_2 to generate Ce^{3+} according to eq 10.

$$2Ce^{4+} + H_2O_2 \rightarrow 2Ce^{3+} + 2H^+ + O_2 \quad (10)$$

Therefore, the H_2O_2 concentration was determined by the UV−visible absorption of Ce^{4+} at 315 nm by eq 11.

$$C(H_2O_2) = {}^1/_2 \times [C_0(Ce^{4+}) - C(Ce^{4+})] \quad (11)$$

The absorbance at λ = 315 nm of the $Ce(SO_4)_2$ solution was detected with UV−vis after adding a known concentration of H_2O_2 solution into the $Ce(SO_4)_2$ solution. The linear relationship between Ce^{4+} concentration and the absorption intensity was established in Figure S18.

Detection of ·OH Species Generated by the Fenton-like Reaction. To evaluate the chemodynamic activity of the developed catalysts, MB was used as an indicator to indicate the production of ·OH. First, a mixture solution containing CoPc-Mn/$Ti_3C_2T_x$-PEG (250 μg mL^{-1}, 0.2 mL), MB (100 μg mL^{-1}, 0.1 mL), and DMF (1.5 mL) were stirred for 5 min to form a homogeneous solution. Subsequently, both H_2O_2 (0.1 mL, 50 mM) and $NaHCO_3$ (0.1 mL, 250 mM) were added into the mixed solution. The generation rates of ·OH at different exposure durations were also detected by monitoring the absorbance changes of MB at 664 nm. In addition, the chemodynamic activities of other samples, including CoPc-TA, CoPc-Mn, CoPc-Mn/$Ti_3C_2T_x$, and CoPc-Mn/$Ti_3C_2T_x$-PEG/AS1411, were also investigated using the same method. Further, the degradation abilities of CoPc-Mn/$Ti_3C_2T_x$-PEG in diverse environments with designed pH values (5.4, 6.4, and 7.4) were determined.

***In Vitro* Photodynamic Effect.** To probe the $^1O_2$ generation efficiency of the samples, DPBF was employed as a probe. First, DPBF (1 mg mL^{-1}, 20 μL) in DMF was freshly prepared, then separately added into each of the sample suspensions (2 mL, 25 μg mL^{-1}), including CoPc-TA, CoPc-Mn, CoPc-Mn/$Ti_3C_2T_x$, $Ti_3C_2T_x$ NSs, CoPc-Mn/$Ti_3C_2T_x$-PEG, and CoPc-Mn/$Ti_3C_2T_x$-PEG/AS1411, with stirring for 5 min in the dark. For $^1O_2$ detection, the UV−vis absorption at 414 nm of sample suspensions was recorded with time intervals of 1 min during irradiation under an 808 nm laser (1 W cm^{-2}). To further study the degradation rate of DPBF, the reaction kinetics was fitted well to a first-order kinetic equation.[80]

$$\ln(C_0/C) = k_a t \quad (12)$$

where k_a, t, C_0, and C are the pseudo-first-order reaction rate constant, reaction time, and DPBF absorbance under a definite irradiation time, respectively.

Intracellular ROS Measurements. Intracellular ROS generation in mouse melanoma B16 cells was detected by DCFH-DA. Typically, B16 cells were seeded into a cell culture dish (1×10^5) and incubated with 2 mL of Roswell Park Memorial Institute (RPMI) 1640 medium for 24 h. Next, fresh 1640 medium containing CoPc-Mn/$Ti_3C_2T_x$-PEG (100 μg mL^{-1}) was added and incubated for 6 h. Wells were then washed with PBS thrice. DCFH-DA (0.1 mL, 20 μM) was introduced to B16 cells with different treatments, including CoPc-Mn/$Ti_3C_2T_x$-PEG, CoPc-Mn/$Ti_3C_2T_x$-PEG + NIR, CoPc-Mn/$Ti_3C_2T_x$-PEG + H_2O_2 (100 μM), and CoPc-Mn/$Ti_3C_2T_x$-PEG + NIR + H_2O_2 (100 μM) for further incubation at 37 °C for 20 min. Finally, CLSM was used for imaging intracellular ROS generation in each well when excited by light at 488 nm.

***In Vitro* Biocompatibility and PDT, PTT, and CDT Performance Assessments.** The cytotoxicity of the CoPc-Mn complex, $Ti_3C_2T_x$ NSs, CoPc-Mn/$Ti_3C_2T_x$, and CoPc-Mn/$Ti_3C_2T_x$-PEG was evaluated using a typical MTT assay against L929 and mouse melanoma B16 cells, separately. Typically, B16 cells (1×10^5) were seeded on 96-well plates, incubated for 12 h (37 °C, 5% CO_2), and then separately incubated with different concentrations of the CoPc-Mn complex, $Ti_3C_2T_x$ NSs, CoPc-Mn/$Ti_3C_2T_x$, and CoPc-Mn/$Ti_3C_2T_x$-PEG suspensions for 24 h. After rinsing gently with PBS thrice, 200 μL of fresh 1640 medium was added and incubated for 12 h at 37 °C. Then the MTT (20 μL, 5 mg mL^{-1} in PBS) was added and cultured in the incubator for 4 h, followed by discharging the mixture medium and adding DMSO. Cell viability was evaluated by the absorbance at 490 and 600 nm using a microplate reader (WD-2102A). The *in vitro* CDT, PTT, and PDT efficiency against B16 cells was evaluated using similar MTT procedures with different treatments, including CoPc-Mn/$Ti_3C_2T_x$-PEG, CoPc-Mn/$Ti_3C_2T_x$-PEG + H_2O_2 (100 μM), CoPc-Mn/$Ti_3C_2T_x$-PEG + NIR (1 W cm^{-2}, 10 min), and CoPc-Mn/$Ti_3C_2T_x$-PEG + NIR (1 W cm^{-2}, 10 min) + H_2O_2 (100 μM), and their efficacy was calculated by detecting the absorbance of each well with a microplate reader.

***In Vivo* and *in Vitro* PA Imaging.** The increasing concentrations of suspensions of CoPc-Mn/$Ti_3C_2T_x$-PEG/AS1411 (20, 40, 80, 100, and 200 μg mL^{-1}) were prepared for *in vitro* PAI with 808 nm laser irradiation, in which the PA signals were obtained on a mouse photoacoustic tomographic system (iThera Medical, InVision 256-TF, Germany). For *in vivo* PAI, 200 μL of CoPc-Mn/$Ti_3C_2T_x$-PEG/AS1411 (200 μg mL^{-1}) was injected intravenously into B16-tumor-bearing mice. Meanwhile, PA images were taken every 1 h postinjection (0, 1, 2, 3, 4, 5, and 6 h) after animals were anesthetized with isoflurane.

Evaluation of the Targeting Ability of CoPc-Mn/$Ti_3C_2T_x$-PEG/AS1411 with B16 Cells. B16 cells and L929 cells were first harvested from cell culture flasks, seeded into 20 mm glass-bottom culture dishes with medium (1 mL), and cultured for 24 h. After the removal of the culture medium, CoPc-Mn/$Ti_3C_2T_x$-PEG/5′-Cy3-labeled AS1411 (100 μg mL^{-1}, 1 mL) was added in every 20 mm glass-bottom culture dish and cultured for 4 h. After rinsing with PBS four times, 1640 medium (1 mL) containing Hoechst 33342 (300 nM, 20 μL) was added into the glass-bottom culture dishes and cultured at 37 °C for 15 min, followed by rinsing with PBS. Finally, cells were immobilized with 4% cold paraformaldehyde for 15 min and rinsed with PBS thrice. The targeting effect of AS1411 in the cellular uptake of CoPc-Mn/$Ti_3C_2T_x$-PEG/AS1411 was evaluated by CLSM (excited at 515 nm).

***In Vivo* Antitumor Treatment Study.** Female BALB/C mice (4−6 weeks) were purchased from Hunan Slaccas Jingda Laboratory Animal Co., Ltd. (Hunan, China) and raised in the SPF animal room. All animal procedures were approved by the Animal Research Ethics Committee of Yanxuan Biotechnology (Hangzhou, China) Co., Ltd. (Document HZYX-2021-011). The B16-tumor-bearing mice models were successfully established when the tumor volume attained ∼70 mm^3. The mice were randomly assigned into four groups, including PBS, PBS + NIR, CoPc-Mn/$Ti_3C_2T_x$-PEG/AS1411, and CoPc-Mn/$Ti_3C_2T_x$-PEG/AS1411 + NIR. Typically, the mice were administered with PBS or CoPc-Mn/$Ti_3C_2T_x$-PEG/AS1411 (200 μL, 200 μg mL^{-1}) by intravenous injection. After 2 h, the groups of PBS + NIR and CoPc-Mn/$Ti_3C_2T_x$-PEG/AS1411 + NIR were treated with NIR laser irradiation (808 nm, 1 W cm^{-2}, 10 min). Body weights and tumor volumes were then measured every other day. After 2 weeks, all dissected tumors and main organs were gathered for further H&E and TUNEL staining analysis.

ASSOCIATED CONTENT

Supporting Information

The Supporting Information is available free of charge at https://pubs.acs.org/doi/10.1021/acsnano.2c12270.

Materials and chemicals; basic characterizations; synthesis of PEG-epoxide; preparations of all solutions; ToF-

https://doi.org/10.1021/acsnano.2c12270
ACS Nano 2023, 17, 11290−11308

SIMS measurements; calculation of PCE; stability of CoPc-Mn/$Ti_3C_2T_x$-PEG/AS1411; *in vivo* biocompatibility study of CoPc-Mn/$Ti_3C_2T_x$-PEG/AS1411; blood serum analysis; immunohistochemical analyses; statistical analysis; FE-SEM, TEM image, and corresponding EDS element maps of the CoPc-TA complex and CoPc-Mn; FE-SEM, TEM image, and corresponding EDS element maps of $Ti_3C_2T_x$ NSs; FE-SEM images of CoPc-Mn/$Ti_3C_2T_x$ and CoPc-Mn/$Ti_3C_2T_x$-PEG; FE-SEM images of CoPc-Mn/$Ti_3C_2T_x$-PEG/AS1411; AFM images of samples; ToF-SIMS depth profiles of CoPc-Mn/$Ti_3C_2T_x$; corresponding EXAFS fitting curves of CoPc-Mn/$Ti_3C_2T_x$ in *k* space and *q* space; EXAFS fitting parameters at the Co K-edge; XRD patterns, FT-IR spectra, UV−vis absorption in DMF, fluorescence spectra, and TGA curves of catalysts; XPS survey scan spectra of catalysts and CoPc-Mn/$Ti_3C_2T_x$-PEG/AS1411; high-resolution XPS spectra of catalysts; high-resolution XPS spectra, FT-IR spectra, and DLS of CoPc-Mn/$Ti_3C_2T_x$-PEG/AS1411; EPR spectra; UV−vis absorption of catalysts in water; temperature elevation curves and infrared thermal images; temperature elevation curves of CoPc-Mn/$Ti_3C_2T_x$-PEG with various power densities; material heating and cooling curve and the $t-(-\ln\theta)$ diagrams; photothermal conversion of all catalysts; photothermal profile of the CoPc-Mn/$Ti_3C_2T_x$ and CoPc-Mn/$Ti_3C_2T_x$-PEG/AS1411; linear relationship between Ce^{4+} concentration and absorption intensity; ESR spectra of catalysts upon irradiation for 10 min in the presence of DMPO-·O_2^- and DMPO-·OH; photographs of O_2 generating phenomenon; degradation of MB by ·OH generated by catalysts; degradation curve of DPBF by catalysts; apparent rate constants of DPBF photodegradation against catalysts; metal ion release profiles of CoPc-Mn/$Ti_3C_2T_x$-PEG at different pH values; cell viabilities of L929 cells incubated with catalysts; time-dependent cellular uptake of CoPc-Mn/$Ti_3C_2T_x$-PEG/AS1411 in B16 cells; blood routine and liver and kidney functions indexes of mice after intravenous injection of CoPc-Mn/$Ti_3C_2T_x$-PEG/AS1411; TUNEL staining images of tumor tissues (PDF)

AUTHOR INFORMATION

Corresponding Authors

Lihong Jing − *CAS Key Laboratory of Colloid, Interface and Chemical Thermodynamics, Institute of Chemistry, Chinese Academy of Sciences, Beijing 100190, China;* orcid.org/0000-0001-6115-2743; Email: jinglh@iccas.ac.cn

Miao Du − *College of Material and Chemical Engineering, Zhengzhou University of Light Industry, Zhengzhou 450001, China*; Email: dumiao@zzuli.edu.cn

Zhihong Zhang − *College of Material and Chemical Engineering, Zhengzhou University of Light Industry, Zhengzhou 450001, China;* orcid.org/0000-0002-5888-4107; Email: 2006025@zzuli.edu.cn

Authors

Fenghe Duan − *College of Material and Chemical Engineering, Zhengzhou University of Light Industry, Zhengzhou 450001, China*

Qiaojuan Jia − *College of Material and Chemical Engineering, Zhengzhou University of Light Industry, Zhengzhou 450001, China*

Gaolei Liang − *College of Material and Chemical Engineering, Zhengzhou University of Light Industry, Zhengzhou 450001, China*

Mengfei Wang − *College of Material and Chemical Engineering, Zhengzhou University of Light Industry, Zhengzhou 450001, China*

Lei Zhu − *College of Material and Chemical Engineering, Zhengzhou University of Light Industry, Zhengzhou 450001, China*

Kevin J. McHugh − *Departments of Bioengineering and Chemistry, Rice University, Houston, Texas 77005, United States*

Complete contact information is available at: https://pubs.acs.org/10.1021/acsnano.2c12270

Author Contributions

The manuscript was written through contributions of all authors.

Notes

The authors declare no competing financial interest.

ACKNOWLEDGMENTS

This work was financially supported by the Excellent Youth Science Foundation of Henan Province, China (No. 202300410494), National Natural Science Foundation of China (22177115, 81671755), the Youth Innovation Promotion Association CAS (Y2022017), and the National Key Research and Development Program of China (2018YFA0208800). All animal procedures were approved by the Animal Research Ethics Committee of Yanxuan Biotechnology (Hangzhou, China) Co., Ltd (Document HZYX-2021-011).

REFERENCES

(1) Rojas, S.; Arenas-Vivo, A.; Horcajada, P. Metal-Organic Frameworks: A Novel Platform for Combined Advanced Therapies. *Coord. Chem. Rev.* **2019**, *388*, 202−226.

(2) Wang, D.; Fang, W.; Huang, C.; Chen, Z.; Nie, T.; Wang, J.; Luo, L.; Xiao, Z. MR Imaging Guided Iron-Based Nanoenzyme for Synergistic Ferroptosis−Starvation Therapy in Triple Negative Breast Cancer. *Smart Mater. Med.* **2022**, *3*, 159−167.

(3) Li, Z.; Gao, Y.; Li, W.; Li, Y.; Lv, H.; Zhang, D.; Peng, J.; Cheng, W.; Mei, L.; Chen, H.; Zeng, X. Charge-Reversal Nanomedicines As a Smart Bullet for Deep Tumor Penetration. *Smart Mater. Med.* **2022**, *3*, 243−253.

(4) Li, Y.; Zhang, P.; Tang, W.; McHugh, K. J.; Kershaw, S. V.; Jiao, M.; Huang, X.; Kalytchuk, S.; Perkinson, C. F.; Yue, S.; Qiao, Y.; Zhu, L.; Jing, L.; Gao, M.; Han, B. Bright, Magnetic NIR-II Quantum Dot Probe for Sensitive Dual-Modality Imaging and Intensive Combination Therapy of Cancer. *ACS Nano* **2022**, *16*, 8076−8094.

(5) Zhang, Y.; Xu, C.; Yang, X.; Pu, K. Photoactivatable Protherapeutic Nanomedicine for Cancer. *Adv. Mater.* **2020**, *32*, 2002661.

(6) Chen, H.; Yang, H.; Zhang, C.; Chen, S.; Zhao, X.; Zhu, M.; Wang, Z.; Wang, Y.; Wo, H. T.; Li, K.; Cheng, Z. Differential Responses of Transplanted Stem Cells to Diseased Environment Unveiled by a Molecular NIR-II Cell Tracker. *Research* **2021**, *2021*, 9798580.

(7) Gilson, R. C.; Black, K. C. L.; Lane, D. D.; Achilefu, S. Hybrid TiO_2−Ruthenium Nano-Photosensitizer Synergistically Produces Reactive Oxygen Species in both Hypoxic and Normoxic Conditions. *Angew. Chem., Int. Ed.* **2017**, *56*, 10717−10720.

(8) Wang, Y.; Wu, W.; Mao, D.; Teh, C.; Wang, B.; Liu, B. Metal−Organic Framework Assisted and Tumor Microenvironment Modulated Synergistic Image-Guided Photo-Chemo Therapy. *Adv. Funct. Mater.* **2020**, *30*, 2002431.

(9) Li, X.; Lee, S.; Yoon, J. Supramolecular Photosensitizers Rejuvenate Photodynamic Therapy. *Chem. Soc. Rev.* **2018**, *47*, 1174−1188.
(10) Teng, K.-X.; Chen, W.-K.; Niu, L.-Y.; Fang, W.-H.; Cui, G.; Yang, Q.-Z. BODIPY-Based Photodynamic Agents for Exclusively Generating Superoxide Radical over Singlet Oxygen. *Angew. Chem., Int. Ed.* **2021**, *60*, 19912−19920.
(11) Wan, Y.; Fu, L.-H.; Li, C.; Lin, J.; Huang, P. Conquering the Hypoxia Limitation for Photodynamic Therapy. *Adv. Mater.* **2021**, *33*, 2103978.
(12) Shi, L.; Zhang, P.; Liu, X.; Li, Y.; Wu, W.; Gao, X.; Liu, B. An Activity-Based Photosensitizer to Reverse Hypoxia and Oxidative Resistance for Tumor Photodynamic Eradication. *Adv. Mater.* **2022**, *34*, 2206659.
(13) Li, L.; Shao, C.; Liu, T.; Chao, Z.; Chen, H.; Xiao, F.; He, H.; Wei, Z.; Zhu, Y.; Wang, H.; Zhang, X.; Wen, Y.; Yang, B.; He, F.; Tian, L. An NIR-II-Emissive Photosensitizer for Hypoxia-Tolerant Photodynamic Theranostics. *Adv. Mater.* **2020**, *32*, 2003471.
(14) Cui, X.; Zhang, J.; Wan, Y.; Fang, F.; Chen, R.; Shen, D.; Huang, Z.; Tian, S.; Xiao, Y.; Li, X.; Chelora, J.; Liu, Y.; Zhang, W.; Lee, C.-S. Dual Fenton Catalytic Nanoreactor for Integrative Type-I and Type-II Photodynamic Therapy Against Hypoxic Cancer Cells. *ACS Appl. Bio Mater.* **2019**, *2*, 3854−3860.
(15) Shi, Z.; Zhang, K.; Zada, S.; Zhang, C.; Meng, X.; Yang, Z.; Dong, H. Upconversion Nanoparticle-Induced Multimode Photodynamic Therapy Based on a Metal−Organic Framework/Titanium Dioxide Nanocomposite. *ACS Appl. Mater. Interfaces* **2020**, *12*, 12600−12608.
(16) Li, S.-H.; Yang, W.; Liu, Y.; Song, X.-R.; Liu, R.; Chen, G.; Lu, C.-H.; Yang, H.-H. Engineering of Tungsten Carbide Nanoparticles for Imaging-Guided Single 1064 nm Laser-Activated Dual-Type Photodynamic and Photothermal Therapy of Cancer. *Nano Res.* **2018**, *11*, 4859−4873.
(17) Sun, J.; Cai, X.; Wang, C.; Du, K.; Chen, W.; Feng, F.; Wang, S. Cascade Reactions by Nitric Oxide and Hydrogen Radical for Anti-Hypoxia Photodynamic Therapy Using an Activatable Photosensitizer. *J. Am. Chem. Soc.* **2021**, *143*, 868−878.
(18) Wang, T.; Zhang, H.; Liu, H.; Yuan, Q.; Ren, F.; Han, Y.; Sun, Q.; Li, Z.; Gao, M. Boosting H_2O_2-Guided Chemodynamic Therapy of Cancer by Enhancing Reaction Kinetics Through Versatile Biomimetic Fenton Nanocatalysts and the Second Near-Infrared Light Irradiation. *Adv. Funct. Mater.* **2020**, *30*, 1906128.
(19) Li, S.-L.; Jiang, P.; Jiang, F.-L.; Liu, Y. Recent Advances in Nanomaterial-Based Nanoplatforms for Chemodynamic Cancer Therapy. *Adv. Funct. Mater.* **2021**, *31*, 2100243.
(20) Liu, C.; Chen, Y.; Zhao, J.; Wang, Y.; Shao, Y.; Gu, Z.; Li, L.; Zhao, Y. Self-Assembly of Copper−DNAzyme Nanohybrids for Dual-Catalytic Tumor Therapy. *Angew. Chem., Int. Ed.* **2021**, *60*, 14324−14328.
(21) Liu, G.; Zou, J.; Tang, Q.; Yang, X.; Zhang, Y.; Zhang, Q.; Huang, W.; Chen, P.; Shao, J.; Dong, X. Surface Modified Ti_3C_2 MXene Nanosheets for Tumor Targeting Photothermal/Photodynamic/Chemo Synergistic Therapy. *ACS Appl. Mater. Interfaces* **2017**, *9*, 40077−40086.
(22) Fan, W.; Lu, N.; Huang, P.; Liu, Y.; Yang, Z.; Wang, S.; Yu, G.; Liu, Y.; Hu, J.; He, Q.; Qu, J.; Wang, T.; Chen, X. Glucose-Responsive Sequential Generation of Hydrogen Peroxide and Nitric Oxide for Synergistic Cancer Starving-Like/Gas Therapy. *Angew. Chem., Int. Ed.* **2017**, *56*, 1229−1233.
(23) Zhang, Y.; Yang, Y.; Jiang, S.; Li, F.; Lin, J.; Wang, T.; Huang, P. Degradable Silver-Based Nanoplatform for Synergistic Cancer Starving-Like/Metal Ion Therapy. *Mater. Horiz.* **2019**, *6*, 169−175.
(24) Feng, L.; Xie, R.; Wang, C.; Gai, S.; He, F.; Yang, D.; Yang, P.; Lin, J. Magnetic Targeting, Tumor Microenvironment-Responsive Intelligent Nanocatalysts for Enhanced Tumor Ablation. *ACS Nano* **2018**, *12*, 11000−11012.
(25) Wang, M.; Chang, M.; Chen, Q.; Wang, D.; Li, C.; Hou, Z.; Lin, J.; Jin, D.; Xing, B. Au_2Pt-PEG-Ce6 Nanoformulation with Dual Nanozyme Activities for Synergistic Chemodynamic Therapy/Phototherapy. *Biomaterials* **2020**, *252*, 120093.
(26) Yan, J.-H.; Meng, W.; Shan, H.; Zhang, X.-P.; Zou, L.-M.; Wang, L.-L.; Shi, J.-S.; Kong, X.-Y. Melanin Nanoparticles Combined with CaO_2 Nanoparticles for Image-Guided Tumor Microenvironment-Responsive Multimodal Therapy. *Acs Appl. Nano Mater.* **2021**, *4*, 1351−1363.
(27) Ding, Y.; Huang, R.; Luo, L.; Guo, W.; Zhu, C.; Shen, X.-C. Full-Spectrum Responsive WO_{3-x}@HA Nanotheranostics for NIR-II Photoacoustic Imaging-Guided PTT/PDT/CDT Synergistic Therapy. *Inorg. Chem. Front.* **2021**, *8*, 636−646.
(28) Xu, Y.; Cheng, C.; Du, S.; Yang, J.; Yu, B.; Luo, J.; Yin, W.; Li, E.; Dong, S.; Ye, P.; Duan, X. Contacts between Two- and Three-Dimensional Materials: Ohmic, Schottky, and p−n Heterojunctions. *ACS Nano* **2016**, *10*, 4895−4919.
(29) Jiao, M.; Portniagin, A. S.; Luo, X.; Jing, L.; Han, B.; Rogach, A. L. Semiconductor Nanocrystals Emitting in the Second Near-Infrared Window: Optical Properties and Application in Biomedical Imaging. *Adv. Opt. Mater.* **2022**, *10*, 2200226.
(30) Liu, J.; Ren, J. C.; Shen, T.; Liu, X.; Butch, C. J.; Li, S.; Liu, W. Asymmetric Schottky Contacts in Van Der Waals Metal-Semiconductor-Metal Structures Based on Two-Dimensional Janus Materials. *Research* **2020**, *2020*, 6727524.
(31) Wu, Y.; Xiong, W.; Wang, Z.; Wang, Y.; Sun, K.-y.; Song, X.; Lv, Z.; Xu, W.; Zhong, W.; Zou, X.; Cai, H.-L.; Wu, X. Self-Assembled MXene-Based Schottky-Junction upon Transition Metal Oxide for Regulated Tumor Microenvironment and Enhanced CDT/PTT/MRI Activated by NIR Irradiation. *Chem. Eng. J.* **2022**, *427*, 131925.
(32) Zhang, X.; Wang, P.; Meng, W.; Cui, E.; Zhang, Q.; Wang, Z.; Zheng, Z.; Liu, Y.; Cheng, H.; Dai, Y.; Huang, B. Photococatalytic Anticancer Performance of Naked Ag/AgCl Nanoparticles. *Chem. Eng. J.* **2022**, *428*, 131265.
(33) Zheng, B.-D.; He, Q.-X.; Li, X.; Yoon, J.; Huang, J.-D. Phthalocyanines As Contrast Agents for Photothermal Therapy. *Coord. Chem. Rev.* **2021**, *426*, 213548.
(34) Lo, P.-C.; Rodríguez-Morgade, M. S.; Pandey, R. K.; Ng, D. K. P.; Torres, T.; Dumoulin, F. The Unique Features and Promises of Phthalocyanines As Advanced Photosensitisers for Photodynamic Therapy of Cancer. *Chem. Soc. Rev.* **2020**, *49*, 1041−1056.
(35) Li, J.; Pu, K. Development of Organic Semiconducting Materials for Deep-Tissue Optical Imaging, Phototherapy and Photoactivation. *Chem. Soc. Rev.* **2019**, *48*, 38−71.
(36) Huang, K.; Li, Z.; Lin, J.; Han, G.; Huang, P. Two-Dimensional Transition Metal Carbides and Nitrides (MXenes) for Biomedical Applications. *Chem. Soc. Rev.* **2018**, *47*, 5109−5124.
(37) Liu, S.; Pan, X.; Liu, H. Two-Dimensional Nanomaterials for Photothermal Therapy. *Angew. Chem., Int. Ed.* **2020**, *59*, 5890−5900.
(38) Tao, W.; Kong, N.; Ji, X.; Zhang, Y.; Sharma, A.; Ouyang, J.; Qi, B.; Wang, J.; Xie, N.; Kang, C.; Zhang, H.; Farokhzad, O. C.; Kim, J. S. Emerging Two-Dimensional Monoelemental Materials (Xenes) for Biomedical Applications. *Chem. Soc. Rev.* **2019**, *48*, 2891−2912.
(39) Zhang, Y.; Cheng, Y.; Yang, F.; Yuan, Z.; Wei, W.; Lu, H.; Dong, H.; Zhang, X. Near-Infrared Triggered Ti_3C_2/g-C_3N_4 Heterostructure for Mitochondria-Targeting Multimode Photodynamic Therapy Combined Photothermal Therapy. *Nano Today* **2020**, *34*, 100919.
(40) Shao, J.; Zhang, J.; Jiang, C.; Lin, J.; Huang, P. Biodegradable Titanium Nitride MXene Quantum Dots for Cancer Phototheranostics in NIR-I/II Biowindows. *Chem. Eng. J.* **2020**, *400*, 126009.
(41) Zhu, Y.; Wang, Z.; Zhao, R.; Zhou, Y.; Feng, L.; Gai, S.; Yang, P. Pt Decorated $Ti_3C_2T_x$ MXene with NIR-II Light Amplified Nanozyme Catalytic Activity for Efficient Phototheranostics. *ACS Nano* **2022**, *16*, 3105−3118.
(42) Geng, B.; Xu, S.; Shen, L.; Fang, F.; Shi, W.; Pan, D. Multifunctional Carbon Dot/MXene Heterojunctions for Alleviation of Tumor Hypoxia and Enhanced Sonodynamic Therapy. *Carbon* **2021**, *179*, 493−504.
(43) Feng, W.; Han, X.; Hu, H.; Chang, M.; Ding, L.; Xiang, H.; Chen, Y.; Li, Y. 2D Vanadium Carbide MXenzyme to Alleviate ROS-Mediated Inflammatory and Neurodegenerative Diseases. *Nat. Commun.* **2021**, *12*, 2203.

https://doi.org/10.1021/acsnano.2c12270
ACS Nano 2023, 17, 11290−11308

(44) Li, G.-L.; Cao, S.; Lu, Z.-F.; Wang, X.; Yan, Y.; Hao, C. FePc Nanoclusters Modified NiCo Layered Double Hydroxides in Parallel with Ti_3C_2 MXene As a Highly Efficient and Durable Bifunctional Oxygen Electrocatalyst for Zinc-Air Batteries. *Appl. Surf. Sci.* **2022**, *591*, 153142.
(45) Heinzerling, J. H.; Mileham, K. F.; Simone, C. B., II The Utilization of Immunotherapy with Radiation Therapy in Lung Cancer: a Narrative Review. *Transl. Cancer Res.* **2021**, *10*, 2596−2608.
(46) Ramachandran, R.; Hu, Q.; Rajavel, K.; Zhu, P.; Zhao, C.; Wang, F.; Xu, Z.-X. Non-Peripheral Octamethyl-Substituted Copper (II) Phthalocyanine Nanorods with MXene Sheets: An Excellent Electrode Material for Symmetric Supercapacitor with Enhanced Electrochemical Performance. *J. Power Sources* **2020**, *471*, 228472.
(47) Ma, H.; Xue, M. Recent Advances in the Photothermal Applications of Two-Dimensional Nanomaterials: Photothermal Therapy and Beyond. *J. Mater. Chem. A* **2021**, *9*, 17569−17591.
(48) Zou, Z.; Wang, Q.; Yan, J.; Zhu, K.; Ye, K.; Wang, G.; Cao, D. Versatile Interfacial Self-Assembly of $Ti_3C_2T_x$ MXene Based Composites with Enhanced Kinetics for Superior Lithium and Sodium Storage. *ACS Nano* **2021**, *15*, 12140−12150.
(49) Yu, X.; Lai, S.; Xin, S.; Chen, S.; Zhang, X.; She, X.; Zhan, T.; Zhao, X.; Yang, D. Coupling of Iron Phthalocyanine at Carbon Defect Site via π-π Stacking for Enhanced Oxygen Reduction Reaction. *Appl. Catal., B* **2021**, *280*, 119437.
(50) Yao, Y.; Ji, K.; Wang, Y.; Gu, Z.; Wang, J. Materials and Carriers Development for Glucose-Responsive Insulin. *Acc. Mater. Res.* **2022**, *3*, 960−970.
(51) Chen, L.; Ye, X.; Chen, S.; Ma, L.; Wang, Z.; Wang, Q.; Hua, N.; Xiao, X.; Cai, S.; Liu, X. Ti_3C_2 MXene Nanosheet/TiO_2 Composites for Efficient Visible Light Photocatalytic Activity. *Ceram. Int.* **2020**, *46*, 25895−25904.
(52) Shi, Z.; Yang, W.; Gu, Y.; Liao, T.; Sun, Z. Metal-Nitrogen-Doped Carbon Materials As Highly Efficient Catalysts: Progress and Rational Design. *Adv. Sci.* **2020**, *7*, 2001069.
(53) Mubarak, N.; Rehman, F.; Ihsan-Ul-Haq, M.; Xu, M.; Li, Y.; Zhao, Y.; Luo, Z.; Huang, B.; Kim, J.-K. Highly Sodiophilic, Defect-Rich, Lignin-Derived Skeletal Carbon Nanofiber Host for Sodium Metal Batteries. *Adv. Energy Mater.* **2022**, *12*, 2103904.
(54) Meng, X.; Liu, X.; Fan, X.; Chen, X.; Chen, S.; Meng, Y.; Wang, M.; Zhou, J.; Hong, S.; Zheng, L.; Shi, G.; Bielawski, C. W.; Geng, J. Single-Atom Catalyst Aggregates: Size-Matching Is Critical to Electrocatalytic Performance in Sulfur Cathodes. *Adv. Sci.* **2022**, *9*, 2103773.
(55) Johnson, C.; Long, B.; Nguyen, J. G.; Day, V. W.; Borovik, A. S.; Subramaniam, B.; Guzman, J. Correlation between Active Center Structure and Enhanced Dioxygen Binding in Co(salen) Nanoparticles: Characterization by In Situ Infrared, Raman, and X-ray Absorption Spectroscopies. *J. Phys. Chem. C* **2008**, *112*, 12272−12281.
(56) Zhu, L.; Liang, G.; Guo, C.; Xu, M.; Wang, M.; Wang, C.; Zhang, Z.; Du, M. A New Strategy for the Development of Efficient Impedimetric Tobramycin Aptasensors with Metallo-Covalent Organic Frameworks (MCOFs). *Food Chem.* **2022**, *366*, 130575.
(57) Huang, Y.; Yu, Y.; Yu, Y.; Zhang, B. Oxygen Vacancy Engineering in Photocatalysis. *Sol. RRL* **2020**, *4*, 2000037.
(58) Lin, F.; Qin, H.; Wang, T.; Yang, L.; Cao, X.; Jiao, L. Few-Layered MoN−MnO Heterostructures with Interfacial-O Synergistic Active Centers Boosting Electrocatalytic Hydrogen Evolution. *J. Mater. Chem. A* **2021**, *9*, 8325−8331.
(59) Arshad, A.; Yun, S.; Shi, J.; Sun, M.; Zafar, N.; Hagfeldt, A. N-Coordinated Bimetallic Defect-Rich Nanocarbons As Highly Efficient Electrocatalysts in Advanced Energy Conversion Applications. *Chem. Eng. J.* **2022**, *435*, 134913.
(60) Zhang, L.; Li, C.-X.; Wan, S.-S.; Zhang, X.-Z. Nanocatalyst-Mediated Chemodynamic Tumor Therapy. *Adv. Healthcare Mater.* **2022**, *11*, 2101971.
(61) Zhang, H.; Zhang, J.; Li, Y.; Jiang, H.; Jiang, H.; Li, C. Continuous Oxygen Vacancy Engineering of the Co_3O_4 Layer for an Enhanced Alkaline Electrocatalytic Hydrogen Evolution Reaction. *J. Mater. Chem. A* **2019**, *7*, 13506−13510.
(62) Wang, Z.; Gai, S.; Wang, C.; Yang, G.; Zhong, C.; Dai, Y.; He, F.; Yang, D.; Yang, P. Self-Assembled Zinc Phthalocyanine Nanoparticles as Excellent Photothermal/Photodynamic Synergistic Agent for Antitumor Treatment. *Chem. Eng. J.* **2019**, *361*, 117−128.
(63) Wu, F.; Yue, L.; Cheng, K.; Chen, J.; Wong, K. L.; Wong, W. K.; Zhu, X. Facile Preparation of Phthalocyanine-Based Nanodots for Photoacoustic Imaging and Photothermal Cancer Therapy In Vivo. *ACS Biomater. Sci. Eng.* **2020**, *6*, 5230−5239.
(64) Li, L.; Yang, Q.; Shi, L.; Zheng, N.; Li, Z.; Li, K.; Qiao, S.; Jia, T.; Sun, T.; Wang, Y. Novel Phthalocyanine-Based Polymeric Micelles with High Near-Infrared Photothermal Conversion Efficiency under 808 nm Laser Irradiation for in Vivo Cancer Therapy. *J. Mater. Chem. B* **2019**, *7*, 2247−2251.
(65) Jia, Q.; Ge, J.; Liu, W.; Zheng, X.; Wang, M.; Zhang, H.; Wang, P. Biocompatible Iron Phthalocyanine-Albumin Assemblies as Photoacoustic and Thermal Theranostics in Living Mice. *ACS Appl. Mater. Interfaces* **2017**, *9*, 21124−21132.
(66) Hou, H.; Wang, Z.; Ma, Y.; Yu, K.; Zhao, J.; Lin, H.; Qu, F. NIR-Driven Intracellular Photocatalytic Oxygen-Supply on Metallic Molybdenum Carbide@N-Carbon for Hypoxic Tumor Therapy. *J. Colloid Interface Sci.* **2022**, *607*, 1−15.
(67) Sui, C.; Tan, R.; Chen, Y.; Yin, G.; Wang, Z.; Xu, W.; Li, X. MOFs-Derived Fe-N Codoped Carbon Nanoparticles as O_2-Evolving Reactor and ROS Generator for CDT/PDT/PTT Synergistic Treatment of Tumors. *Bioconjugate Chem.* **2021**, *32*, 318−327.
(68) Sang, D.; Wang, K.; Sun, X.; Wang, Y.; Lin, H.; Jia, R.; Qu, F. NIR-Driven Intracellular Photocatalytic O_2 Evolution on Z-Scheme Ni_3S_2/$Cu_{1.8}S$@HA for Hypoxic Tumor Therapy. *ACS Appl. Mater. Interfaces* **2021**, *13*, 9604−9619.
(69) Wang, J.-H.; Li, S.; Chen, Y.; Dong, L.-Z.; Liu, M.; Shi, J.-W.; Li, S.-L.; Lan, Y.-Q. Phthalocyanine Based Metal−Organic Framework Ultrathin Nanosheet for Efficient Photocathode toward Light-Assisted Li−CO_2 Battery. *Adv. Funct. Mater.* **2022**, *32*, 2210259.
(70) Peng, C.; Yang, X.; Li, Y.; Yu, H.; Wang, H.; Peng, F. Hybrids of Two-Dimensional Ti_3C_2 and TiO_2 Exposing {001} Facets toward Enhanced Photocatalytic Activity. *ACS Appl. Mater. Interfaces* **2016**, *8*, 6051−6060.
(71) Yu, K.; Tang, L.; Cao, X.; Guo, Z.; Zhang, Y.; Li, N.; Dong, C.; Gong, X.; Chen, T.; He, R.; Zhu, W. Semiconducting Metal−Organic Frameworks Decorated with Spatially Separated Dual Cocatalysts for Efficient Uranium(VI) Photoreduction. *Adv. Funct. Mater.* **2022**, *32*, 2200315.
(72) Cheng, Y.; Kong, X.; Chang, Y.; Feng, Y.; Zheng, R.; Wu, X.; Xu, K.; Gao, X.; Zhang, H. Spatiotemporally Synchronous Oxygen Self-Supply and Reactive Oxygen Species Production on Z-Scheme Heterostructures for Hypoxic Tumor Therapy. *Adv. Mater.* **2020**, *32*, 1908109.
(73) Xiao, R.; Zhao, C.; Zou, Z.; Chen, Z.; Tian, L.; Xu, H.; Tang, H.; Liu, Q.; Lin, Z.; Yang, X. In Situ Fabrication of 1D CdS Nanorod/2D Ti_3C_2 MXene Nanosheet Schottky Heterojunction toward Enhanced Photocatalytic Hydrogen Evolution. *Appl. Catal., B* **2020**, *268*, 118382.
(74) Shiraishi, Y.; Shiota, S.; Hirakawa, H.; Tanaka, S.; Ichikawa, S.; Hirai, T. Titanium Dioxide/Reduced Graphene Oxide Hybrid Photocatalysts for Efficient and Selective Partial Oxidation of Cyclohexane. *ACS Catal.* **2017**, *7*, 293−300.
(75) Sun, Q.; Wang, Z.; Liu, B.; He, F.; Gai, S.; Yang, P.; Yang, D.; Li, C.; Lin, J. Recent Advances on Endogenous/Exogenous Stimuli-Triggered Nanoplatforms for Enhanced Chemodynamic Therapy. *Coord. Chem. Rev.* **2022**, *451*, 214267.
(76) Kang, Y.; Mao, Z.; Wang, Y.; Pan, C.; Ou, M.; Zhang, H.; Zeng, W.; Ji, X. Design of a Two-Dimensional Interplanar Heterojunction for Catalytic Cancer Therapy. *Nat. Commun.* **2022**, *13*, 2425.
(77) Chen, X.; Ge, X.; Qian, Y.; Tang, H.; Song, J.; Qu, X.; Yue, B.; Yuan, W.-E. Electrospinning Multilayered Scaffolds Loaded with Melatonin and Fe_3O_4 Magnetic Nanoparticles for Peripheral Nerve Regeneration. *Adv. Funct. Mater.* **2020**, *30*, 2004537.
(78) Dong, Z.; Liang, X.; Zhang, Q.; Luo, S.; Liu, H.; Wang, X.; Sai, N.; Zhang, X. Folic Acid Deficiency Enhances the Tyr705 and Ser727

Phosphorylation of Mitochondrial STAT3 in In Vivo and In Vitro Models of Ischemic Stroke. *Transl. Stroke Res.* **2021**, *12*, 829−843.
(79) Guo, M.; Zhang, M.; He, D.; Hu, J.; Wang, X.; Gong, C.; Xie, X.; Xue, Z. Comb-Like Solid Polymer Electrolyte Based on Polyethylene Glycol-Grafted Sulfonated Polyether Ether Ketone. *Electrochim. Acta* **2017**, *255*, 396−404.
(80) Lara-Ramos, J. A.; Diaz-Angulo, J.; Machuca-Martínez, F. Use of Modified Flotation Cell As Ozonation Reactor to Minimize Mass Transfer Limitations. *Chem. Eng. J.* **2021**, *405*, 126978.

https://doi.org/10.1021/acsnano.2c12270
ACS Nano 2023, 17, 11290−11308